Macro Scale Physical Model of Nanoindentation on Vertically Aligned Carbon Nanotube Forests

by

Geoffrey F. Ebeling

Submitted to the Department of Mechanical Engineering in Partial Fulfillment of the Requirements for the Degree of

Bachelor of Science

at the

Massachusetts Institute of Technology

[June 2004]

May 2004

Signature of Author.....
Department of Mechanical Engineering
May 10, 2004

Certified by.....
Mary Boyce
Professor of Mechanical Engineering
Thesis Supervisor

Accepted by.....
Ernest G. Cravalho
Chairman, Undergraduate Thesis Committee

Macro Scale Physical Model of Nanoindentation on Vertically Aligned Carbon Nanotube Forests

by

Geoffrey F. Ebeling

Submitted to the Department of Mechanical Engineering
On May 10, 2004 in Partial Fulfillment of the
Requirements for the Degree of Bachelor of Science in
Mechanical Engineering

ABSTRACT

Currently the process of nanoindentation is being explored as a reliable means of determining the mechanical properties of carbon nanotubes (CNTs) and the constituent tubes of vertically aligned carbon nanotube (VACNT) forests. Under indentation, each CNT can be modeled as a cantilevered beam subjected to deflection from the penetration of the indenter. The resistance to indentation is the result of the cumulative bending of the VACNTs. Using beam theory, the effective bending stiffness is determined by fitting the mechanical model to the indentation force-penetration curves. In order to validate the process of nanoindentation as a means of determining the elastic modulus of CNTs, a macro scale physical model was built using cylindrical rods of a known material and used to help explain some of the interactions of the tubes and indenter. Two models and two indenters were built to explore these effects and how they changed between models and indenters. The models demonstrated that for the indenter with a low face angle, the process was rather accurate with corresponding errors of 7% and 15%. When using a flatter indenter on both models, particularly the model with the higher areal density of tubes, demonstrated the inaccuracy of the process as a means for determining the elastic modulus of the material. Such a result was due to abnormal spikes in the data that were observable and attributed to tube interaction with the edge of the indenter. The process of indentation is reliable when the aberrations are minimal or are identifiable in the indentation force versus indentation depth curves and thus can be easily discounted.

The process of scratching was also explored. For scratching the indenter is fixed at a certain indentation height and the tube forest is then horizontally displaced and thus further deflects the tubes. The tubes enter three phases of contact, which subsequently affect the behavior of the scratching force versus distance curves. The macro scale model was used to validate the predicted behavior of CNTs. In general the scratching data supported the behavior of a three phase interaction between the tubes and indenter and the subsequent curves. For more accurate results and numerical comparisons, the forests need to be displaced using a constant speed linear stage and measured against distance.

Thesis Supervisor: Mary Boyce

Title: Professor of Mechanical Engineering

1. Introduction

Nanotechnology is a rapidly growing field of engineering that has received a tremendous amount of research over the past decade. Carbon nanotubes (CNTs) are of particular interest due to their recently explored electrical and mechanical properties. CNTs possess a very high elastic modulus and strength due to their cylindrical and nearly defect free carbon hexagonal lattice structure and could be used in many electronic and thermal devices. Although CNTs offer tremendous opportunities, many of the techniques used to determine the material properties of CNTs have led to inconsistent results and have proven to be difficult to perform.

Carbon nanotubes are composed of the wrapping of single atomic layer sheets and exist as single-walled carbon nanotubes (SWCNTs) and concentrically nested multi-walled carbon nanotubes (MWCNTs). Currently, there are a few methods used to produce CNTs, such as carbon-arc discharge, laser ablation of graphite and chemical vapor deposition. One CNT production technique produces vertically aligned Carbon nanotubes (VACNTs), also referred to as nanoforests or nanograss. Currently multi-walled VACNTs are grown onto a substrate, whereby the substrate is coated with a thin layer metal catalyst; the layer is heated, resulting in the breakup of the metal layer into small islands; a plasma is infused by plasma enhanced chemical vapor deposition (PECVD), which reacts with the islands, under controlled pressured and temperature conditions, acting to grow the CNTs. Figure 1 shows a few examples of VACNTs.

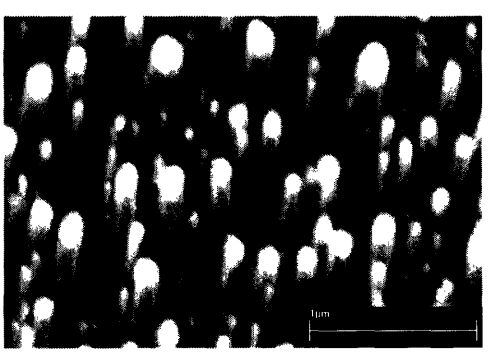

(a)

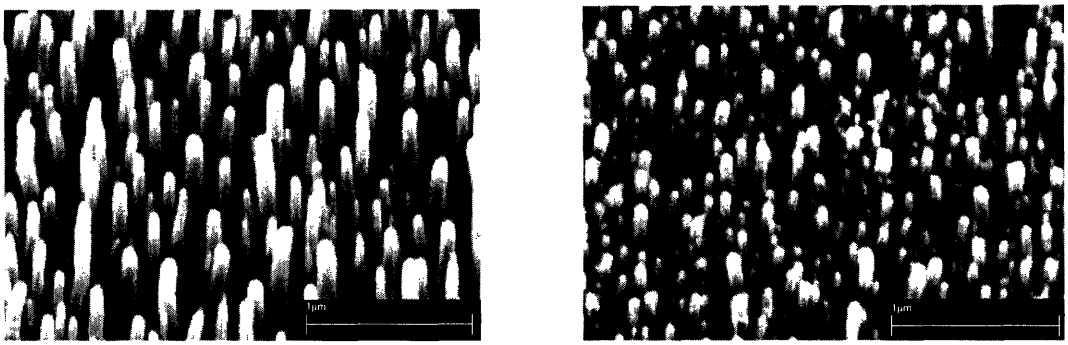

(b) (c)

Figure 1: VACNT forests tilted by 25° to provide better visualization: (a) Sample A, (b) Sample B, (c) Sample B [1].

Before exploring these VACNT forests many researchers first looked at isolated CNTs in order to attempt to measure their material properties, specifically the modulus of elasticity, reducing the experimental data using two differing theoretical approaches [1].

The first approach to determine the mechanical properties of CNTs capitalizes on the use of classical beam theory. In applying beam theory, isolated CNTs are considered cylindrical rods subjected to bending using various experimental methods to support and load the CNT. Measurement of some form of load versus displacement response and/or vibration response enable the determination of an effective bending stiffness, $(EI)_{eff}$ of the CNT, where E_t^b is the effective bending modulus and I_{eff} is the effective moment of inertia of the nanotube. The effective moment of inertia is approximated as:

$$I_{eff} = \pi(D_o^4 - D_i^4)/64\,, \tag{1}$$

where D_{o} is the outer diameter of the nanotube and D_{i} is the inner diameter. Thus the effective bending modulus is defined as:

$$E_t^b \approx \frac{(EI)_{eff}}{I_{eff}}\,. \tag{2}$$

Several methods of testing the bending of SWCNTs and MWCNTs have been used to explore displacement - load behavior and, using beam theory, determined the modulus of

CNTs. Treacy et al. (1996) measured the amplitude of thermally induced vibrations of isolated CNTs, which was measured within a TEM. Taking the CNT as a solid cylinder and using beam theory, an effective bending modulus of 1.28 ± .59 TPa was found [2]. Wong et al. (1997) dispersed MWCNTs on a smooth flat substrate and cantilevered the nanotubes by deposition of an array on this substrate. An AFM was then used to scratch the surface at the free end of the nanotubes and the subsequent lateral force and displacement were measured. The particular test led to effective elastic modulus of MWCNTS of 1.28 ± 0.59 TPa [3]. Poncharal et al. (1999) electrically induced static and mechanical deflection in cantilevered MWCNTs, which were excited at their resonant frequencies and found a modulus close to 1 TPa [4]. Salvetat et al. (1999) deposited CNTs on a well polished alumina ultra-filtration membrane on which a CNT was occasionally placed over a pore and subjected to bending by nanoindentation. An effective bending modulus of 0.81 ± 0.41 TPa was found [5].

As is apparent by the results reported above, a quite considerable range in effective bending modulus was found depending on the particular approach. The first major challenge in testing CNTs is found in their simple size scale, which imperative in their name, is on the nanoscale ($10^{-9} m$) level. Such an incredibly small scale makes it difficult to accurately achieve the desired loading, to properly measure the length, as well as appropriately place CNTs in desired locations or arrangements. Moreover, the structure of multi-walled nanotubes requires a more in-depth analysis regarding the nested tube structure of MWCNTs and the single-atomic layer nature of each tube wall [6-7].

Researches have found, using molecular dynamics (MD) simulations that SWCNTs have internal strain energy per carbon atom to be proportional to $1/R^2$, where R is the radius of the nanotube. Such a dependency led researches to believe that the wall of the nanotube mechanically replicates shell theory, which has subsequently become the second approach used in determining the material properties of nanotubes. Coupled with molecular dynamics, simulations of SWCNTs in compression and tension revealed a wall membrane stretching stiffness, C, equal to 58.2 $eV/atom$ and a wall bending stiffness, D, of 2.23 $eVA^2/atom$. Due to the atomic layer nature of a CNT wall, assigning a particular value for wall thickness is a bit of an ambiguous process. Since the internal

strain energy per carbon atom of a CNT had a similar value relative to unstrained graphite sheet, many have used a wall thickness, t_{wall}=0.340 nm, that corresponded to the graphite interlayer spacing. Using a classical approach with the mentioned values of C and t_{wall} gives an elastic wall modulus of 1.06 TPa. Shell theory predicts that:

$$D = \frac{t_{wall}^3 E_t^w}{12\left(1-\upsilon^2\right)}, \tag{3}$$

where υ is the Poisson ratio calculated from the diameters of the nanotubes stretched in simulations. However, using t_{wall} = 0.340 nm with a wall modulus of 1.06 TPa in equation (3) gives a bending stiffness, D, almost twenty five times greater than that found using MD results. Yakobsen et al. (1996) used previous ab initio and semi-empirical MD results to fit data to shell theory to determine the wall thickness, t_{wall}=0.066 nm, and thus elastic wall modulus, E_t^w =5.5 TPa, which correctly determined the wall bending stiffness [8]. The results also supported that the SWCNTs could be treated as a beam with effective bending stiffness before local instabilities occurred. Several further experiments were done to confirm the use of shell theory. Zhou et al. (2000) used electronic band theory in conjunction with a tight-binding (TB) model to estimate the strain energy and Young's modulus. The total energy was then calculated by accounting for the occupied band electrons. The subsequent total energy was then broken down into the rolling energy, compressing and stretching energy, and the bending energy, all of which were used to obtain a wall bending stiffness of 5.1 TPa and wall thickness of 0.074 nm [9]. Tu and Ou-Yang (2002) used a local density approximation model, while Kundin et al. (2001) used further ab initio energy calculations that also proved consistent with the shell theory [10]. The behavior of MWCNTs can be modeled using the previous results with a continuum elastic shell theory provided that the inter-wall spacing, s, of the CNT walls remains constant due to strong Van der Waals forces and that there is a very low (and thus negligible) shear interaction between the walls. The implications of these conditions on theory surrounding MWCNTs will be further explored later in the thesis.

While researchers were able to determine the properties of isolated nanotubes, a method was still needed to reliably measure the properties of the relative uniformity of

constituent nanotubes in a VACNT forest, providing an excellent alternative for such measurements compared to the complexity of insulating, securing and loading single CNTs. Qi et al. (2002) used a method implementing nanoindentation. The density of the CNT forest is determined by counting the number of nanotubes projected by a Scanning Electron Microscopy (SEM) and dividing by the surface area of the image. The length, L, and diameter, D, of the sample are determined by measuring thirty randomly selected CNTs in this projection. A diamond, three-sided pyramid, is then cantilevered over the forest.

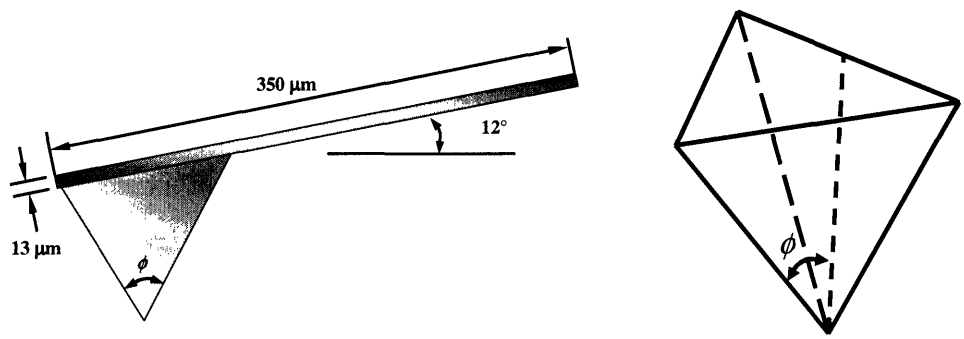

Figure 2: Cantilevered three-sided pyramid indenter [1].

The cantilever is initiated into a tapping mode with a resonant frequency of 55 to 60 kHz using a Digital Instrument Dimension 3100 Scanning Probe Microscopy (SPM) and used to scan the forest and locate a desired area for indentation. The indenter is then lifted to a preset distance about the top of the surface and begins indentation until a desired penetration depth is reached. The results yield penetration depth versus the indentation resistance force. The resistance is due to the combined bending of nanotubes as they are engaged by the indenter. The non-linear relationship is used to deduce the effective bending stiffness, $(EI)_{eff}$, from which the model accounting for the multi-walled structure of CNTs used to obtain the effective bending modulus, E_t^b, wall modulus, E_t^w, and an effective axial modulus, E_t^a. Table 1 shows the results of the three sample VACNT forests (see figure 1) used to determine the material properties of CNTs. The data appears to be in good agreement with the previously mentioned values determined for the

various moduli [1]. The values for $(EI)_{eff}$, E_t^b, E_t^w, and E_t^a were obtained using the model of this indentation process that is discussed in the next section.

Table 1: Properties determined for the three nanoindentation samples [1].

Sample	Average $\overline{D}_o(nm)$	Average $L(nm)$	N	$(EI)_{eff}\left(N(nm)^2\right)$	$E_t^b(TPa)$	$E_t^w(TPa)$	$E_t^a(TPa)$
A	104	930	143	5.2	0.91	4.14	0.90
B	90	1150	123	4.0	1.24	5.61	1.23
C	55	570	72	0.51	1.14	5.11	1.11

The three samples all had various average diameter, $\overline{D}_o$, and length, L, and various number of membrane walls, N, which partially account for the differing effective bending stiffness.

2. Model of Nanoindentation

2.1 Theoretical model of nanoindentation for VACNT forests

The individual nanotubes present in a VACNT forest are individually subjected to bending deformation and each offer a resistance to the indentation because of their resistance to bending. Summing all of these resistance forces for a given penetration depth leads to the total penetration resistance force versus penetration curve. Thus each individual nanotube may be broken down into a 2D schematic to determine their constituent role in the indentation process. The tip of the indenter is initially at a distance, h_o, above the surface of the nanotubes. However, for measurement purposes the penetration depth, h, is measured from the top of the VACNT forest. As the indenter moves further into the forest it first touches a nanotube at a depth of h_1 (see figure 3).

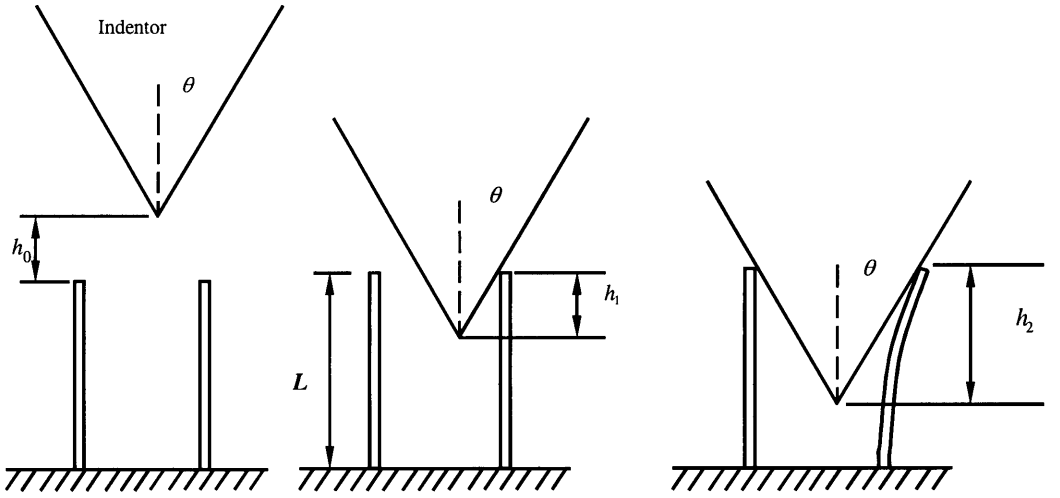

Figure 3: Schematic of nanoindentation and contact between indenter and nanotube [1].

As the indenter penetration continues, the indenter comes into contact with a second nanotube at a depth h_2. Thus the *ith* tube is touched at a depth of h_i. The deflection of the beam can then be related to the penetration depths by using the geometry of the indenter. With a tip angle, θ, the tip deflection, w_o, of the *ith* nanotube is defined as:

$$w_o = (h - h_i)\tan\theta. \qquad (4)$$

Classical beam theory is then used to relate the deflection, as determined by indenter geometry, to the indentation force. A free body diagram of the interaction between the indenter and a single nanotube is shown in figure 4.

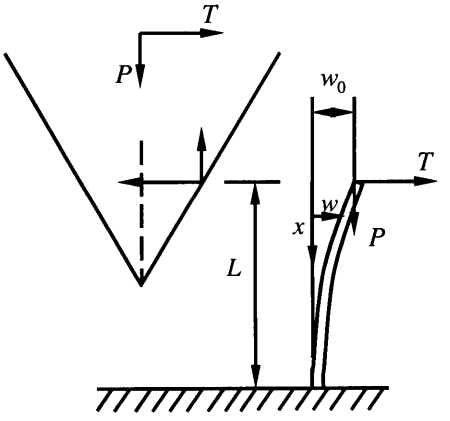

Figure 4: Force-body diagram (FBD) of nanotube and indenter [1].

The force exerted on the tube is composed of the penetration force, P_i, and the lateral force, T_i, which produces a moment on the tube at a distance, x, along the tube that is equal to,

$$M = -T_i x - P_i(w_o - w), \tag{5}$$

where w is the deflection of the tube with respect to distance along the tube. The curvature, κ, of a deflected tube is given by,

$$\kappa = \frac{d^2 w}{dx^2}. \tag{6}$$

Classical beam theory for a cantilevered beam then gives the relationship between the moment and curvature:

$$(EI)_{eff} \frac{d^2 w}{dx^2} = T_i x + P_i y, \tag{7a}$$

$$\text{where } y = (w_o - w). \tag{7b}$$

Since the nanotube is found to have a strong interaction at the base of the tube where it bonds to the substrate, a clamped boundary condition may be applied:

$$y\big|_{x=0} = 0, \tag{8a}$$

$$\frac{dy}{dx}\Big|_{x=L} = 0, \tag{8b}$$

$$w\big|_{x=l} = 0. \tag{8c}$$

Integrating equation (7) twice, using the boundary condition of equation (8), produces:

$$Y = \frac{T_i}{P_i k_i \cos k_i L} \sin k_i x - \frac{T_i}{P_i} x, \tag{9}$$

$$\text{where } k_i = \sqrt{P_i / (EI)_{eff}}.$$

Thus the deflection is defined as:

$$w = w_o - \frac{T_i}{P_i k_i \cos k_i L} \sin k_i x + \frac{T_i}{P_i} x. \tag{10}$$

While equation (10) relates the deflection to any point along the tube, it is more desirable to know the max deflection, which occurs at the tip of the tube. Implementing the boundary condition found in equation (8c), the tip deflection can be reduced to:

$$w_o = \frac{T_i}{P_i}\left(\frac{\tan k_i L}{k_i} - L\right). \tag{11}$$

The lateral force and penetration force, as defined in the free body diagram are related by:

$$T_i = \frac{P_i}{\tan\theta}. \tag{12}$$

Combining equation (4), (11) and (12), the penetration depth and penetration force for a single nanotube can be related as:

$$h = h_i + \frac{1}{(\tan\theta)^2}\left(\frac{\tan k_i L}{k_i} - L\right). \tag{13}$$

Finally, the tip of the indenter comes into contact with n nanotubes depending on the location of the tip. The total indentation force is,

$$P_{total} = \sum_{i=1}^{n} P_i \,. \tag{14}$$

It must be noted that when $h \leq h_i$ there is no indentation force and thus P_{total} is equal to zero until the tip of the indenter touches the first tube.

The value of h_i, for an individual nanotube, depends on the position of the indenter relative to that tube. Geometric considerations for each individual forest could be used to determine such relations but would require lengthy and difficult calculations. Rather, statistical data from a large number of indentation tests was used to determine the average value, $\overline{h_i}$, for the *ith* tube in contact with the tip. The data was collected for an indenter with a face angle, with respect to the vertical, of 21.6°. For a depth h the area of the cross-section of the indenter and a nanotube with a diameter of D_o was found to be:

$$A = 0.813h^2 + 4.11D_o h + 3.141D_o^2 \,. \tag{15}$$

The cross-sectional area of the indenter and the number of nanotubes, i, in contact with the indenter at a given depth, $\overline{h_i}$, are further defined by their areal density, m, of a particular VACNT forest:

$$i = Am \,. \tag{16}$$

It is now possible to determine the height of contact for the *ith* tube, based on the statistical data and consequently the necessary means to fit theoretical calculations to gathered experimental data. The effective bending stiffness, $(EI)_{eff}$, is thus determined by fitting the theoretical data to the experimental data for indentation force versus indentation depth [1].

2.2 Application of indentation model for various changes in governing parameters

A matlab program (see Appendix A) for the indentation theory is used to graph indentation force versus depth for changes in the various parameters. Figure 5 Shows curves for changes in effective bending stiffness, $(EI)_{eff}$, while the length, L, and areal density, m, are held constant.

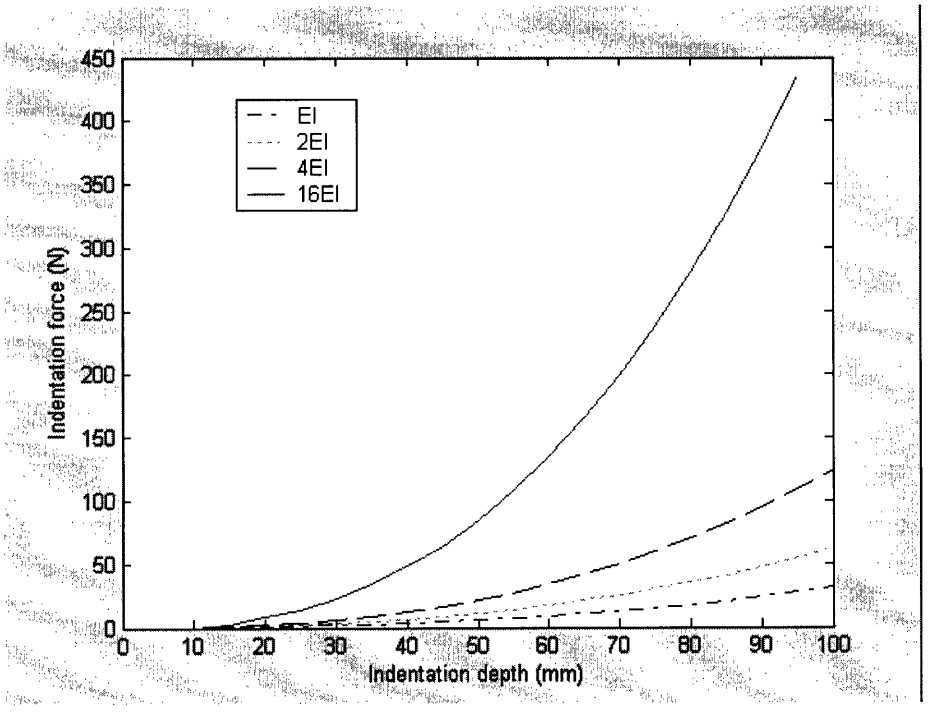

Figure 5: Indentation force versus indentation depth for various EI, while L and m are held constant.

The curves show that as EI increases the curves correspondingly shift up. Figure 6 shows curves for the case when L and EI are varied while m remains constant. The graph shows that when L is increased, for constant EI and m, the curves shift down. However, they show that increasing L has a greater effect on the curves than increasing EI. Consider the case when the bending stiffness is quadrupled the reference stiffness, EI, and the length is twice the reference length.

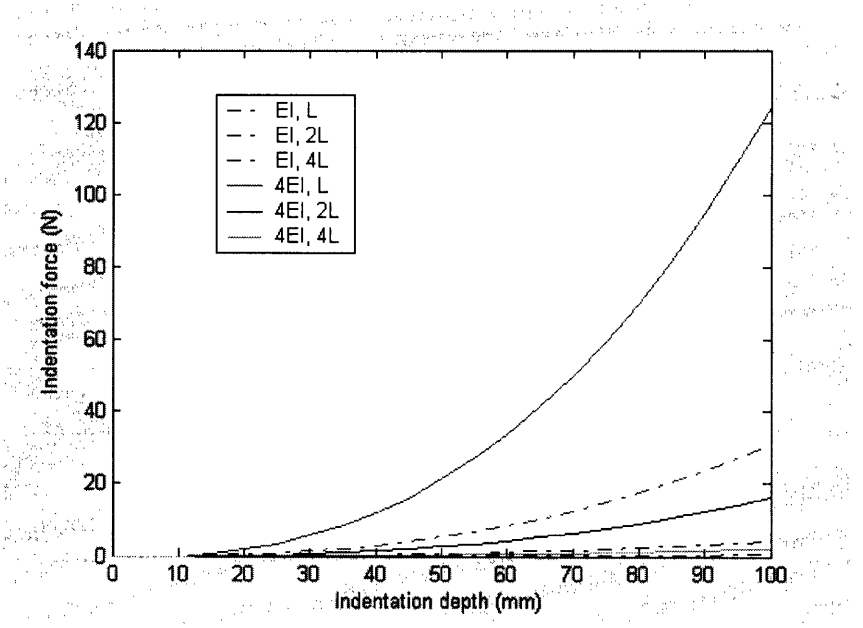

Figure 6: Indentation force versus indentation depth for various L and EI, while m is held constant.

Here we see that quadrupling the EI does not counter double the length since the curve is shifted down from the reference curve of EI and L. Thus changing the length has a greater effect than changing the bending stiffness.

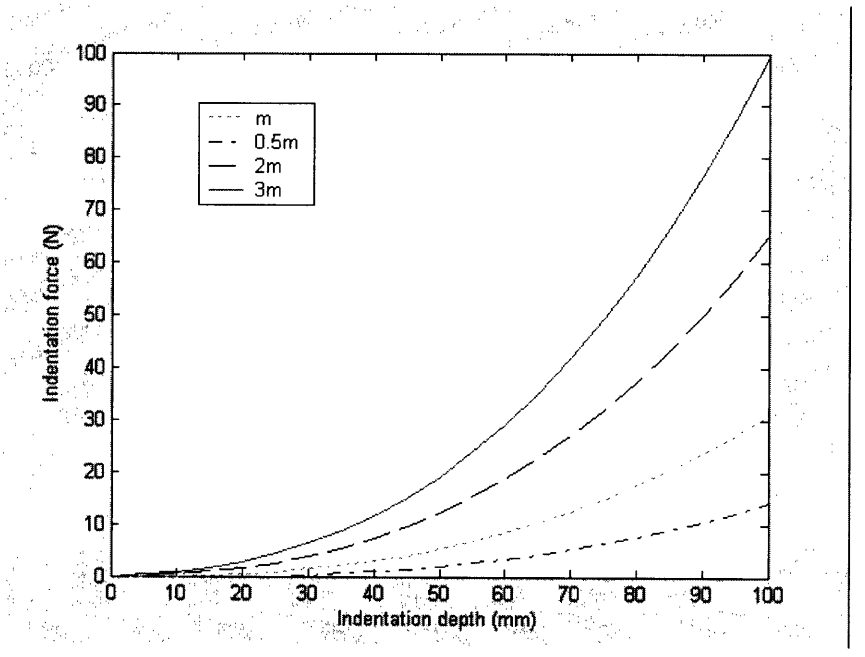

Figure 7: Indentation force versus indentation depth for various m, while L and EI are held constant.

Figure 7 shows the case when the areal density is varied, and L and EI remain constant. The curves clearly indicate that as m increases the force increases corresponding to depth.

2.3 Axial and wall modulus for constituent MWCNTs

The effective bending modulus, the wall modulus and effective axial modulus can all be deduced from the effective bending stiffness, determined from fitting the theoretical data to actual indentation force versus indentation depth data. The effective bending modulus is easily determined, whether the nanotubes are single- or multi-wall nanotubes. Simply divide the stiffness by the effective moment of inertia, as seen in equation (2). It can be reduced to:

$$E_t^b = \frac{(EI)_{eff}}{I_{eff}} = \frac{64(EI)_{eff}}{(\pi(D_o^4 - D_i^4))} \approx \frac{64(EI)_{eff}}{(\pi D_o^4)}, \qquad (17)$$

where D_i is the inner diameter and can be approximated to be equal to zero due to its small value relative to the outer diameter. As described earlier, the membrane walls of a MWCNT can be described to be concentric walls with a wall thickness, t, and an inter-wall spacing, s, which remain constant during bending, a crucial factor in the following theory. The wall interactions have led researches to believe that the effective bending stiffness of MWCNTs can be thus approximated as the sum of the bending stiffness of the walls. Isolating a particular constituent wall of a multi-wall CNT, the moment of inertia, I_j, and cross-sectional area, A_j, for the *jth* wall can be defined as:

$$I_j = \frac{\pi}{64}\left[D_j^4 - (D_j - 2t)^4\right], \qquad (18a)$$

$$A_j = \frac{\pi}{4}\left[D_j^2 - (D_j - 2t)^2\right], \qquad (18b)$$

where D_j is the outer diameter of the *jth* wall. The outer diameter of each wall does not need to be individually known, only the outer diameter of the outer wall, in other words the outer diameter of the tube. Then the outer diameter of the *(j-1)th* wall is found by:

$$D_{j-1} = D_j - 2s\,. \tag{19}$$

The effective bending stiffness can now be redefined in terms of the wall modulus and the axial stiffness, $(EA)_{eff}$, can be defined and are:

$$(EI)_{eff} = \sum_{j=1}^{N} E_t^w I_j = E_t^w \sum_{j=1}^{N} I_j \;, \tag{20a}$$

$$(EA)_{eff} = \sum_{j=1}^{N} E_t^w A_j = E_t^w \sum_{j=1}^{N} A_j \;. \tag{20b}$$

Recall that N is the total number of walls in a constituent MWCNT and that the wall modulus is assumed uniform for all walls. Correspondingly equation (20a) can be solved in terms of the desired wall modulus:

$$E_t^w = \frac{(EI)_{eff}}{\sum_{j=1}^{N} I_j}. \tag{21}$$

Once the wall modulus is determined the axial modulus can be found. The effective axial modulus found is further defined as:

$$(EA)_{eff} = E_t^a A_t\,, \tag{22}$$

where A_t is the total cross-sectional area of the tube. Thus the axial modulus is:

$$E_t^a = \frac{E_t^w \sum_j^N A_j}{A_t}. \tag{23}$$

The formulations of the wall axial modulus and the tube axial modulus are dependent on the accuracy of the inter-wall spacing and thickness of the walls. Without the Van der Waals forces and low shear stress between the walls the previous correlations would be inaccurate. It must also be noticed that the inter-wall spacing has been found over a range of 0.34 to 0.39 nm and the wall thickness a range of 0.066 to 0.075 nm. Thus the values determined for the each modulus hold somewhat of a potential error due to the ranges in values. However, the results provide rather accurate values, as shown in comparison with other experimental and theoretical results, in a lower cost and less time consuming manner.

3. Design and construction of macro scale physical model of nanoindentation on VACNT forests

3.1 Model design

A macro scale physical model of the nanoindentation is desired in order to give a better visual representation of the process and to verify the application and efficacy of this approach as a method for determining tube modulus from the indentation force-penetration data. Specifically, the model is used to show how the tubes interact with the indenter and each other and how that relates to the experimental force-penetration data gathered for VACNT forests. Also the model would help further validate the accuracy of fitting theory to experimental data when the material properties are previously known. Different indenter geometries and tube parameters are then used to show how such behavior is correspondingly affected.

Proper material and dimensional selections were needed to accurately make a model of nanoindentation and also meet a few predetermined conditions. An axial load test machine (TA.XTPlus Texture Analyser), shown in figure 8, is used to provide the

vertical indentation force. However, this particular axial test machine can only provide a maximum of 30 kg.

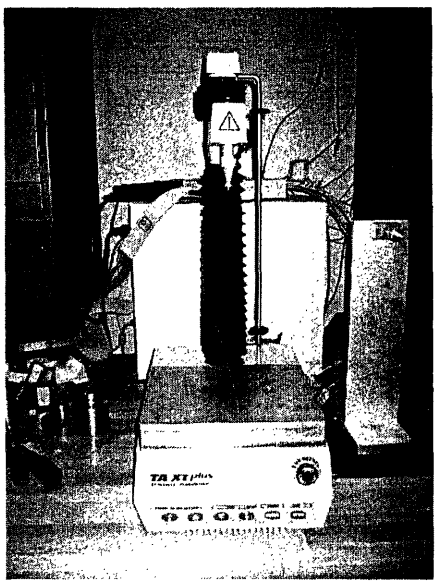

Figure 8: Axial test machine.

Also the nanoforest model plus the indenter had to fit within the size constraints of the axial machine. An indenter with a face angle, with respect to the vertical, of 21.6° was to be built to indent a depth about three quarters the length of the tubes. Thus considering the constraints of the axial test machine, an initial constraint for the height of the tubes was determined to be around 7 inches, although smaller heights were explored and eventually used. Cylindrical rods come in standard diameters for each material and for this experiment a maximum constraint for the diameter of 0.5 inches was considered in order to minimize materials and to make sure that the ratio of length to diameter could be close to those of actual CNTs tested.

A Matlab program (see appendix A) was created using the theory of indentation on a forest of tubes, as described in chapter 2, where the elastic modulus and tube length, diameter and the areal density of the forest could be varied. The program then output the corresponding graph of the indentation force versus the penetration depth corresponding to various input parameters. All types of materials, with various elastic moduli, were tested using the maximum constraints determined above. It was found that material with an elastic modulus less than 3 GPa met the force requirements of the axial test machine.

A stress analysis was then done in order to make sure the materials being considered would not yield under the large deflections.

Materials exposed to large deformations are subject to plastic deformation, which occurs when the maximum stress of the material exceeds the stress yield limit. A cylindrical rod considered to be cantilevered at one end and subjected to a bending force has an axial stress, σ_{xx_a}, and bending stress, σ_{xx_b} and thus the total maximum stress, $\sigma_{xx_{\max}}$, is defined as:

$$\sigma_{xx_{\max}} = \sigma_{xx_b} + \sigma_{xx_a} . \tag{24}$$

The maximum bending stress of the rod at any axial section is:

$$\sigma_{xx_b} = -\frac{M(\frac{D_o}{2})}{I_{eff}}, \tag{25}$$

where M is the moment on the rod as defined in equation (5). The maximum stress of a cantilevered beam subjected to an end load occurs at the point where the rod is cantilevered, where the moment is the largest. Thus, referring to the free body diagram found in figure 4, the bending stress can be broken down into:

$$\sigma_{xx_b} = \frac{(TL + Pw_o)\cdot\left(D_o/2\right)}{\pi\left(D_o^4/64\right)}. \tag{26}$$

The axial strain of the rod is defined as:

$$\sigma_{xx_a} = \frac{F}{A_{eff}} = -\frac{P}{\pi\cdot\left(D_o^2/4\right)}. \tag{27}$$

Using equations (24), (26) and (27) the maximum stress of the tubes for the various material and geometric selections was also determined and compared to that material's yield strength that was being analyzed.

In taking into consideration all of the previous constraints, Teflon was chosen as the material. Teflon under the geometric constraints would not only meet the force criteria of the axial test machine but also would not yield, and is still susceptible to being machined despite its' low modulus and is very affordable. An initial model, model A, design was decided upon with a diameter of 0.375 inches and a length 4.9 inches, which roughly corresponded to a length to diameter ratio used in experiments by Qi et al [1]. The indenter, which is dependent on the length of tubes used, correspondingly determined the area of the plate, which had to be large enough to encompass the entire indenter (table 2 and 3 show the parameters for both models and both indenters constructed).

Table 2: Parameters for the tube forest models.

Model	Base Size (in^2)	Tube Height (in)	Tube Diameter (in)	Areal Density (tubes/in^2)
A	6x12	4.9	0.375	0.7
B	6x8	5.75	0.1875	1.46

Table 3: Indenter parameters.

Indenter	Base Length (in)	Height (in)	Face Angle
1	5.5	4.01	21.6
2	6	0.79	65.3

An arbitrary areal density of 0.7 tubes/in^2 was chosen, which limited the number of tubes needed but was also high enough where more than a couple of tubes contacted the indenter during a typical indentation. The initial design can be seen in figure 9.

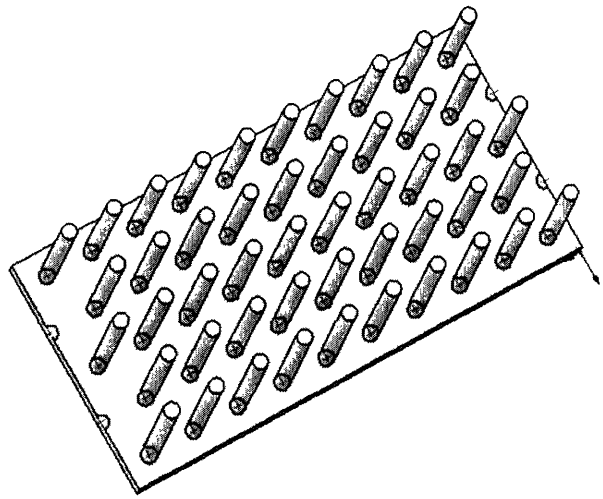

Figure 9: Design for Model A.

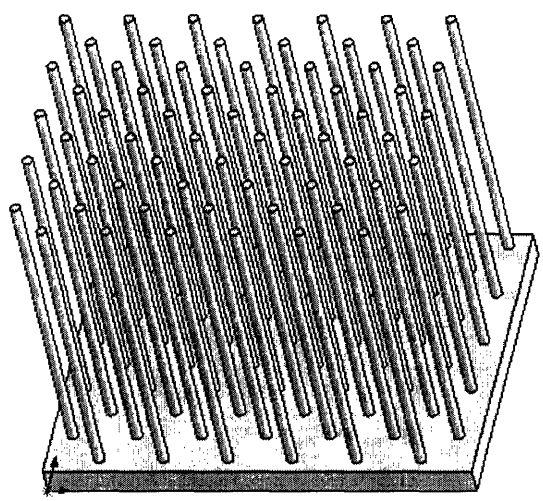

Figure 10: Design for Model B.

A second sample, shown in figure 10, was made using a different diameter, length and areal density and one which could be compared with the first sample and also would be susceptible to scratching.

The scratching of VACNTs have yet to be explored, but scratching is a likely cause for mechanical failure of these nanoforests and will be discussed further in the next chapter. In order for scratching to occur the tubes need to sustain even greater deflections without exceeding the force and yield requirements. Considering these constraints, the diameter of the tubes for the second model, model B, was 3/16 inch with a length of 5.75 inches, an areal density of 1.46 tubes/in^2. The tubes for this sample were arranged in a face centered cubed (FCC) spatial pattern for symmetry.

3.2 Construction of Model

The Teflon tubes used for the model were threaded and screwed into an aluminum plate. The aluminum plate for each sample was prepared using a mill to drill the appropriate holes and then tapped. The two assembled models can be seen in figure 11 (a)-(b). The indenters were made out of sheets of aluminum. An aluminum sheet was cut into two appropriate pieces that each represented two faces of the indenter.

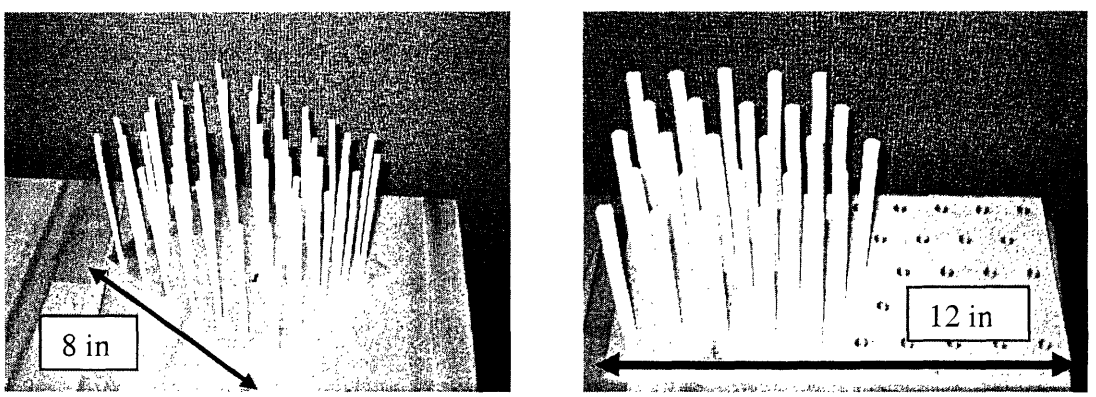

(a) (b)

Figure 11: (a) model B; (b) model A.

Each piece was then folded to the appropriate angle, depending on which indenter was being built. Then the two pieces were joined together through welding. The excess material from the welding was then sanded down to reveal smooth faces and sharp edges. A pen nut, matching a connector screw for the axial machine, was attached to the base face of the indenter.

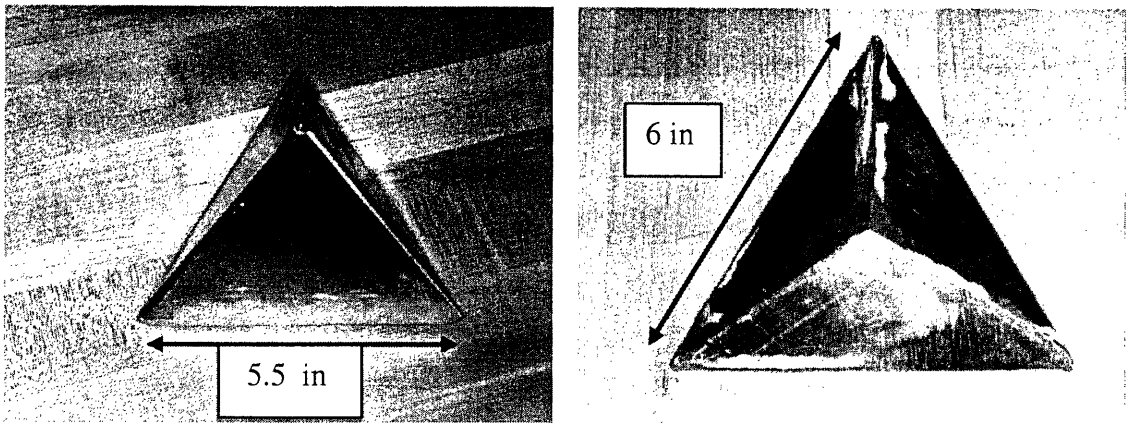

(a) (b)

Figure 12: Macro indenters; (a) indenter with a face angle, with respect to the vertical, of 21.6°; (b) indenter with a face angle, with respect to the vertical, of 65.3°.

The same process was done for both the indenters with corresponding face angles of 21.6° and 65.3°, shown in figure 12 (a)-(b).

4.0 Results and discussion of model indentation

4.1 Experimental observations and indentation aberrations

The results from the model certainly follow the general trend of nanoindentation on actual nanoforests. Model results for the case of imposed indentation with both an indenter with an edge angle of 21.6° and 65.3° all showed parabolic trends in the indentation force-indentation depth behavior as seen in nanoindentation. Figure 13 shows a typical indentation force versus depth for nanoindentation of a VACNT forest.

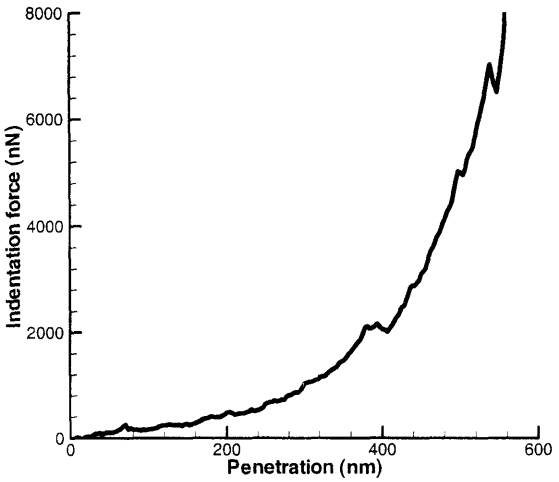

Figure 13: Force-penetration curve for a nanoindentation experiment.

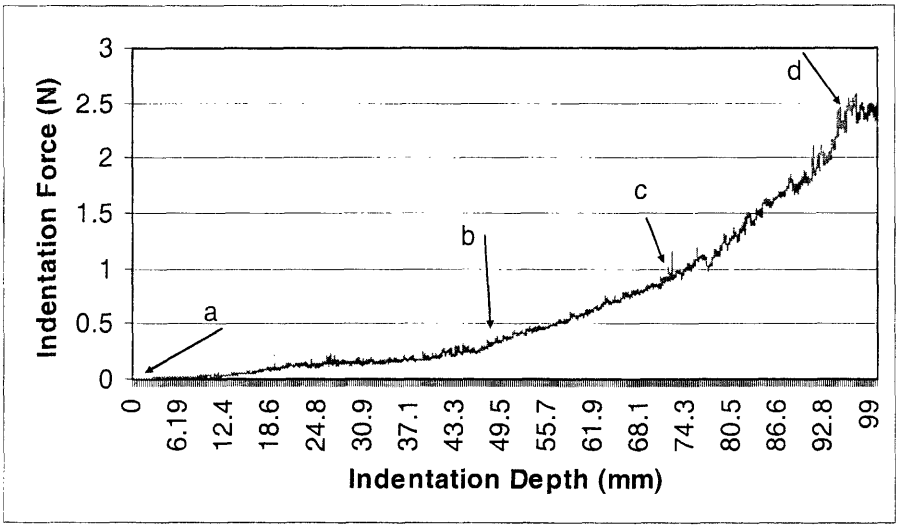

(a)

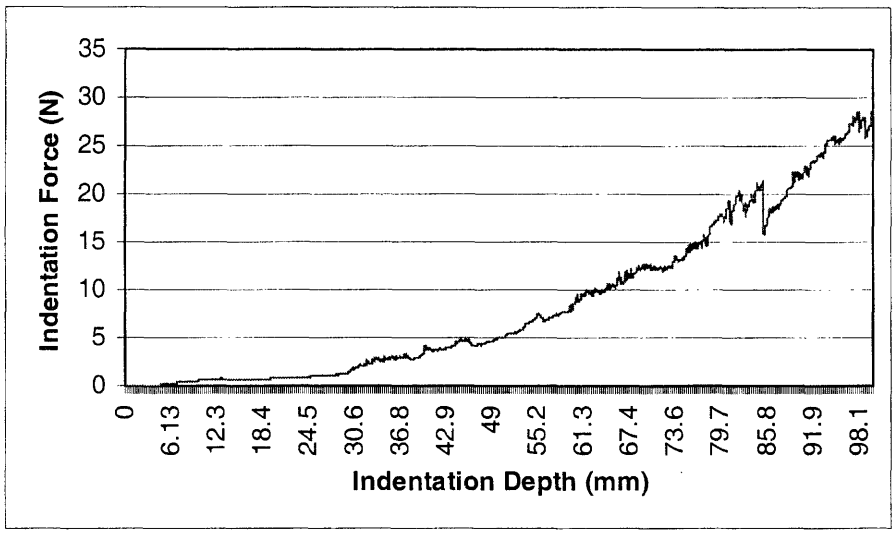

(b)

Figure 14: Indentation force versus depth while using the indenter with the face angle, relative to the vertical, of 21.6°; (a) model B; (b) model A. The sequential markings along model B curve correspond to sequential photos taken and shown in figure 15.

Figure 14 shows the results of indentation done on physical models A and B with the 21.6° indenter. In order to give a visual representation of the process, sequential photos were taken, which correspond to the points marked along the curve in figure 14 (a). Point *a* along the curve is the start position and zero tubes touch the indenter. At point *b*, *c*, and *d* there are 9, 16 and 20 tubes, respectively, in contact with the indenter.

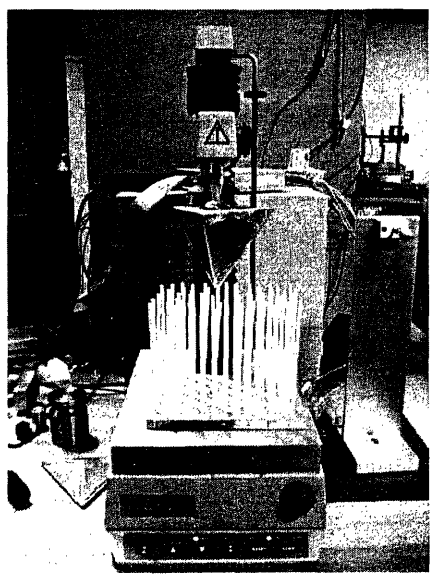

(a)

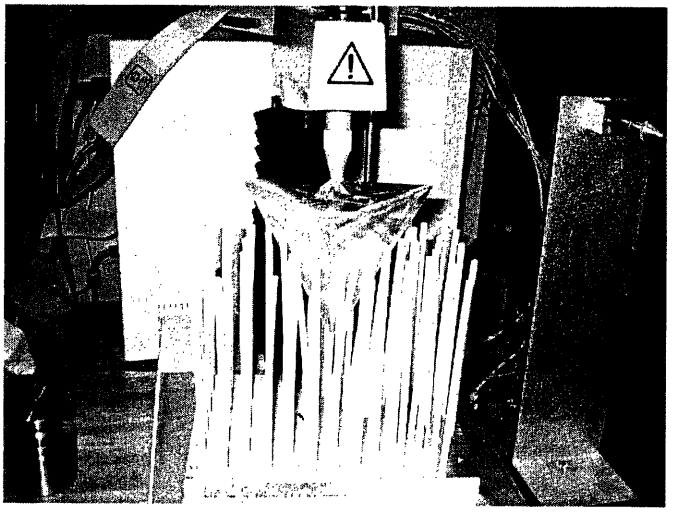

(b)

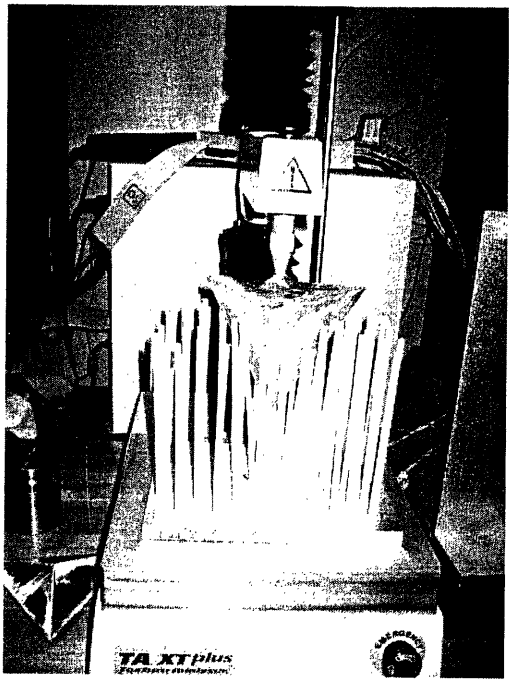

(c)

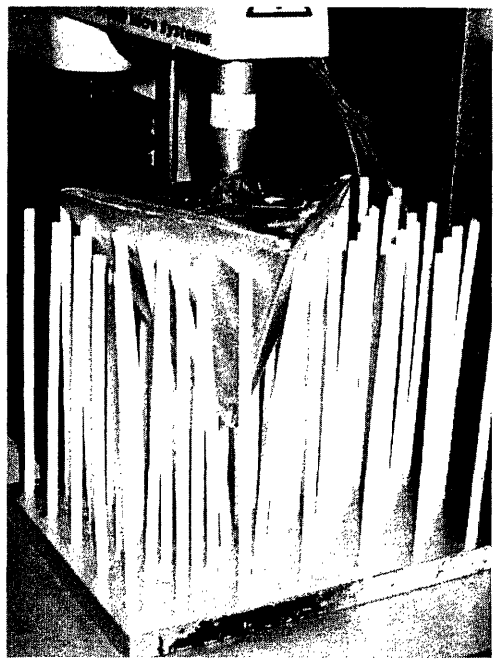

(d)

Figure 15: Photos taken of indentation on model B with the 21.6° indenter and correspond to the markings in figure 14 (a); (a) a; (b) b; (c) c; (d) d.

The same process was also done for the two models and the indenter with a face angle, relative to the vertical, of 65.3°. The results are shown in figure 16 and the corresponding photos for model A can be seen in figure 17.

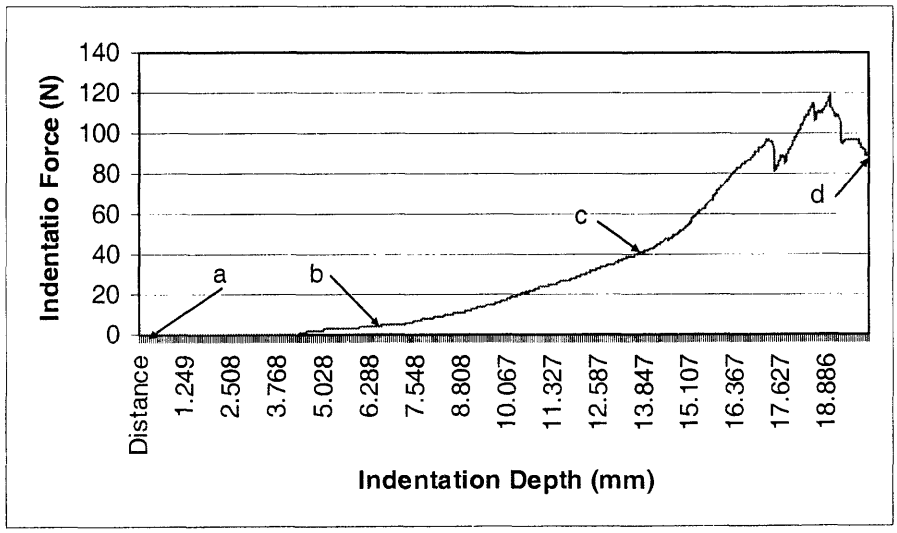

(a)

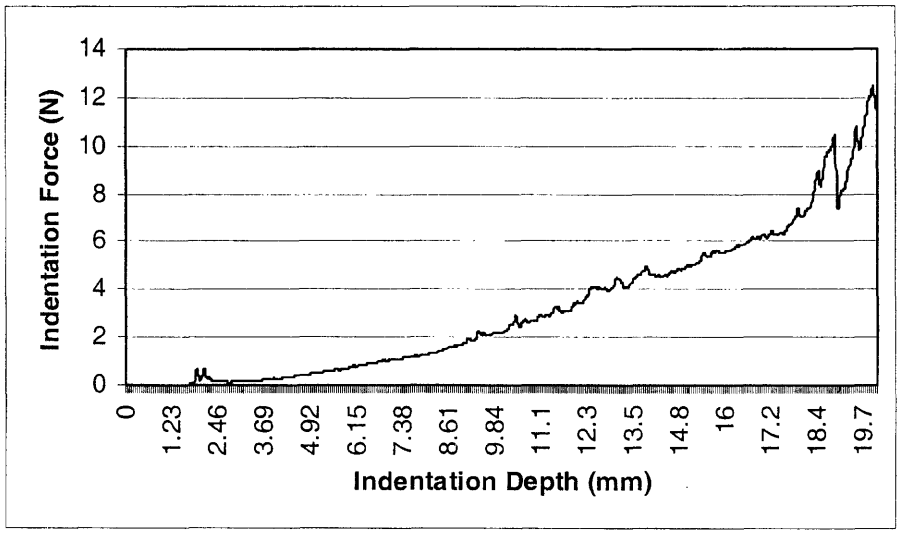

(b)

Figure 16: Indentation force versus depth while using the indenter with the face angle, relative to the vertical, of 65.3°; (a) models A; (b) B;. The sequential markings along model A's curve correspond to sequential photos taken and shown in the next figure.

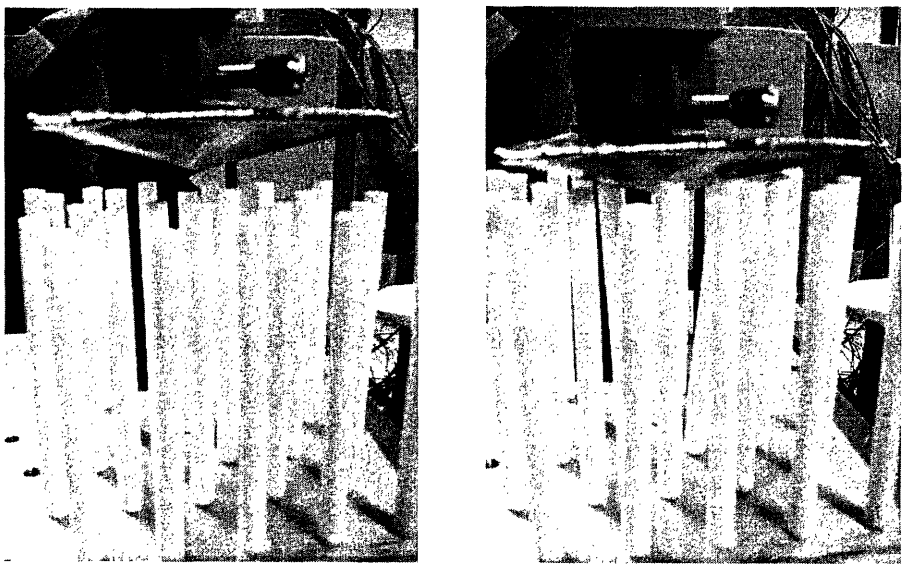

(a) (b)

(c) (d)

Figure 17: Photos taken of indentation on model B with the 21.6° indenter and correspond to the markings in figure 16 (a); (a) a; (b) b; (c) c; (d) d.

The data supports, for both indenters, that increasing the areal density and diameter shifts the force versus depth curves up, while increasing the length shifts the curve down and has a greater effect. Similarly, the flatter indenter created steeper exponential behavior and thus greater indenter forces relative to penetration for both models A and B.

As can be seen in figures 14 and 16 there are apparent aberrations in the data, with some of the tests for each potential situation having considerably more noise than others. Through observation of the experiments, some of the aberrations were clearly identifiable. Almost all major defects were the result of the interaction between a tube and the edge of an indenter. One of the most common problems occurred between the edge of the 21.6° indenter and the tubes. Often a tube first came into contact with an edge of the indenter as opposed to a face. The tube initially deflected as it would on a normal face but at a greater rate due to the large angle of the edge. Then as the deflection, and subsequently indentation force, increased the tube became increasingly unstable on the round edge and eventually slipped off onto a face. The tube returned to a less deflected state and as a result decreased in force. The indentation force verses indentation depth would subsequently return to its normal parabolic path. The effect can be seen in figure 18 and is shown for model A and B.

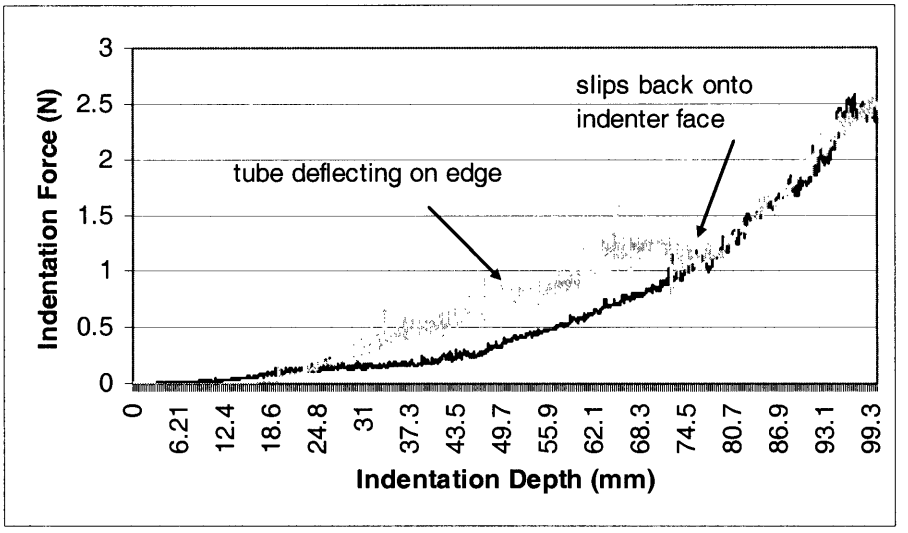

(a)

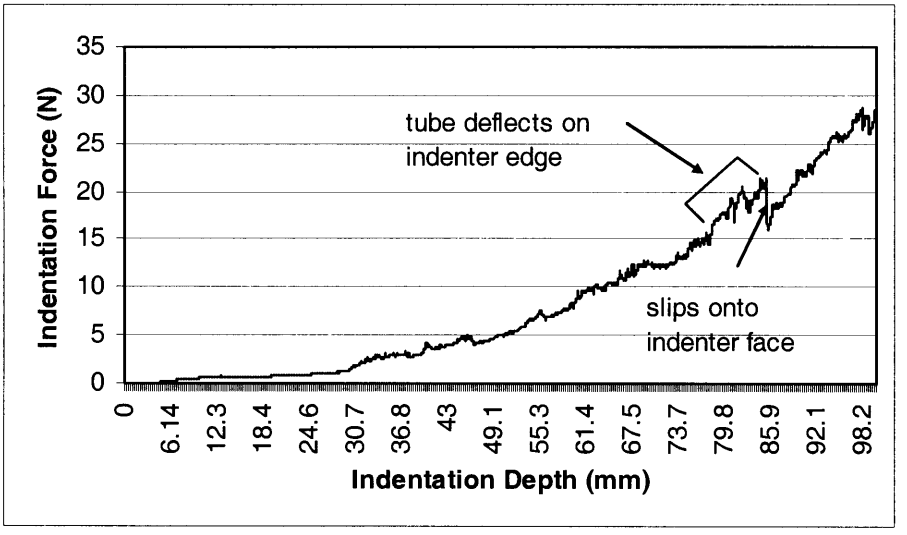

(b)

Figure 18: Indentation force verses depth shows edge instability, (a) model B exposed to 21.6° indenter; (b) model A exposed to 21.6° indenter.

Model A contained the thicker and shorter tubes. As depth increased; the indentation force consequently increased at a greater rate than model B, as shown by equation (13). The greater the resistance to deflection the more unstable the tube became. Thus, as is seen in figure 18 (b), the tube slipped off of the edge over a smaller change in indentation depth. Similarly compiled tests done on nanoforests show very similar behavior, as seen in figure 13, and would suggest, although not conclusively, that nanoindentation on CNTs has very similar interactions with the edge of a 21.6° indenter.

The 65.3° indenter also had some edge effects with the tubes. Instead of deflecting, the tubes in model B, when contacting the indenter at the edge, compressed because of high normal force due to the large face angle. This compression caused greater changes in resistance force, than deflecting along the edge, as seen in figure 19. The tubes continued to compress until they slipped off the edge and back on the face where normal deflection ensued. The compression behavior was a lot more noticeable and caused larger aberrations than the previously described edge effect.

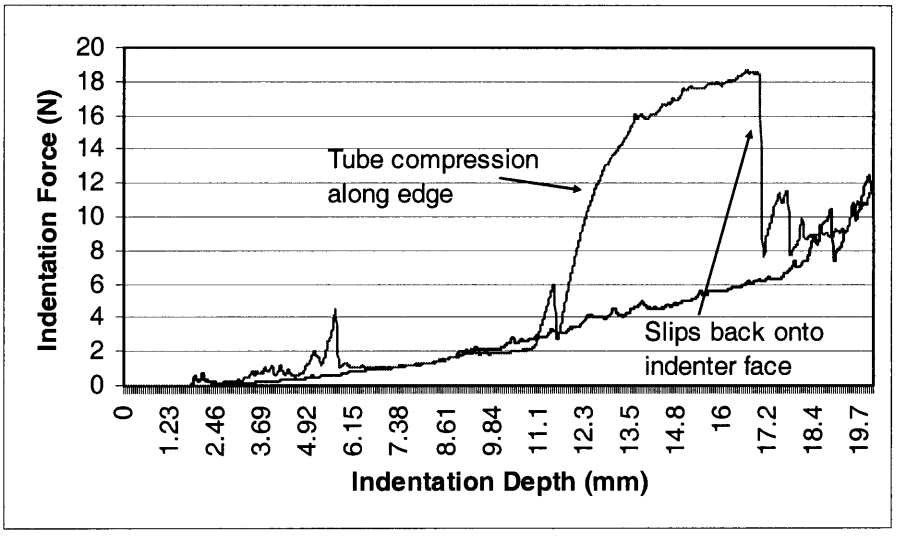

Figure 19: Compression behavior for model B and indenter 65.3°.

The compression also made it difficult to consistently obtain clean results and proved that this combination of tube size and indenter was unreliable. Such combinations may also come into play with actual nanoforest indentation tests and should be avoided when trying to determine material properties.

While compression occurred in model B, the longer and thinner tube model, compression very rarely occurred with model A. The shorter, thicker tubes often slipped off the edge right as any compression behavior began to occur. Overall the results were more consistent. The major aberrations found in model A, while using the 65.3° indenter, actually had little to do with edge effects. A few spots on the indenter were a bit rough and when a tube contacted the area of higher friction it often began to briefly compress. The tubes slipped off of the area and returned to the appropriate deflected state when the

lateral contact force was enough to overcome the increased friction. Thus when doing nanoindentation, surface impurities, relative in size to that of the tube diameter, of the indenter must be taken into consideration.

For model B, which had the larger areal density, as the indentation depth increased, tubes often began to come into contact with one another. Tubes often first began to deflect as a result of contact with an already deflected tube and not the indenter. The tube not in contact with the indenter was very unstable in the cylindrical tubes and as its deflection increased became increasingly unstable. Similar to edge effects, the tube eventually slipped off of the other tube and came to rest on the indenter (see Figure 20).

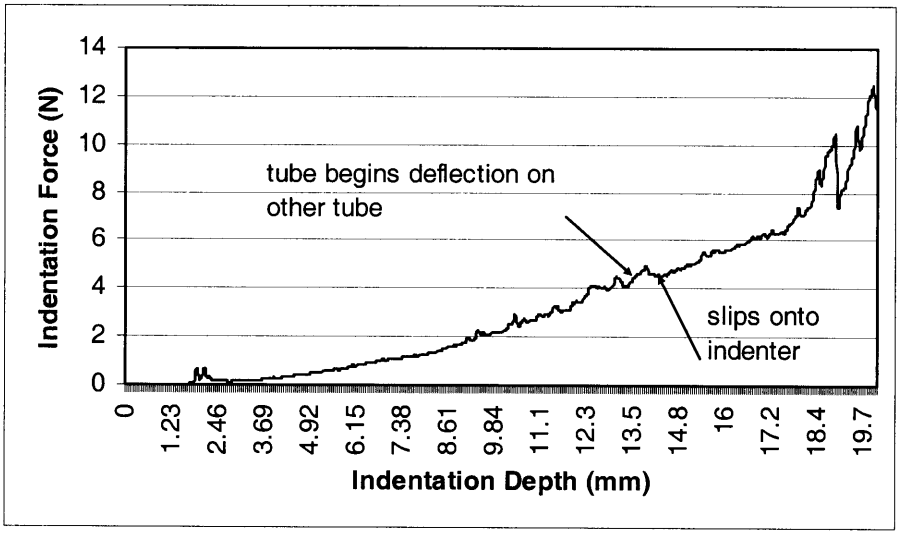

Figure 20: Indentation Force versus depth for model B and 65.3° indenter and demonstrates tube-tune interaction.

As a result the tube was in a less deflected state and small decreases in indentation force were visible. Since the tubes were rather small compared to the scale of deflection they were subjected to, these decreased spikes in force were rather minimal. Had model A, with the larger diameter tubes, been built with a greater areal density this effect would have been more noticeable.

In general the aberrations were apparent in some of the tests and not the others due to changes in indent location. As the location changed, and thus the depth at which the first tube contacted the indenter change, new and different aberrations occurred and. Figure 21 shows all the tests done and the average of the test for model A and the 65.3°

indenter. Appendix B shows the other tests for all other possible cases of models and indenters. Notice that indenter location plays a much bigger role for flatter indenters and greater areal densities, as there are greater shifts in the experimental curves.

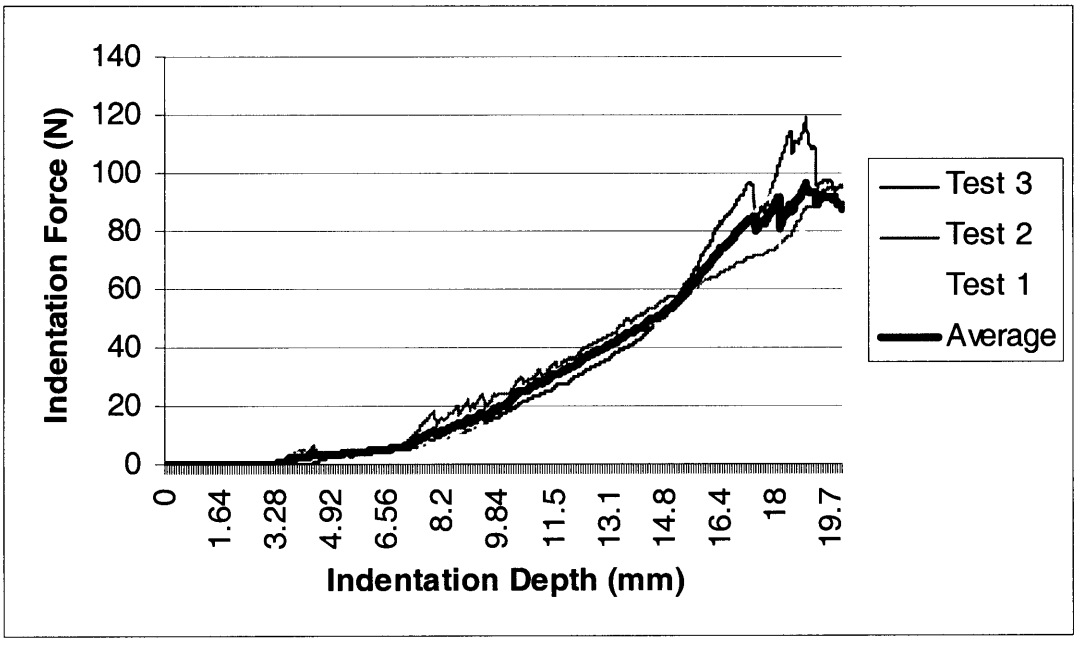

Figure 21: Indentation force versus depth for model B with 65.3° indenter and includes all tests taken and average of tests.

4.2 Fitting experimental data to theoretical predictions

The models were largely used to verify the efficacy of deducing CNT moduli from nanoindentation. While the elastic moduli was already known for Teflon, the theoretical model, using the known modulus, was compared to the actual experimental results. Three out of four of the indenter and model combinations certainly showed that the theory, dependent on the known modulus, was in good agreement with the tests. For example, for model A the error of the force values between the theoretical and experimental data at a depth of 40 mm was 10% and at depth of 80mm was 4%. The theoretical data was also adjusted to better match the experimental data and thus give the elastic modulus the experiments would suggest. The 21.6° indenter provided the most accurate results, as can be seen in figure 22. Using the particular indenter provided the least amounts of aberrations, which when they did occur were rather minimal. The error

associated with fitting the theory to the results by adjusting the elastic modulus was approximately 15% for model B and 7% for model A (see Table 4).

Table 4: Elastic modulus as determined by experimental data for models A and B with 21.6° indenter.

Model	Known Modulus of Teflon (GPa)*	Modulus as Determined by Experimental Data (GPa)	Error
A	0.7	0.65	7%
B		0.8	15%

*Modulus given by material supplier but also confirmed by doing indent on a single tube and comparing to theoretical model(see Appendix C).

Although the errors are noticeable, they are not high enough to refute the indentation approach. However, the same level of accuracy was not seen using the flatter, 65.3° indenter. When applied to model A, the theory mirrored the experimental data, but certainly with a higher degree of error, as seen in Figure 23.

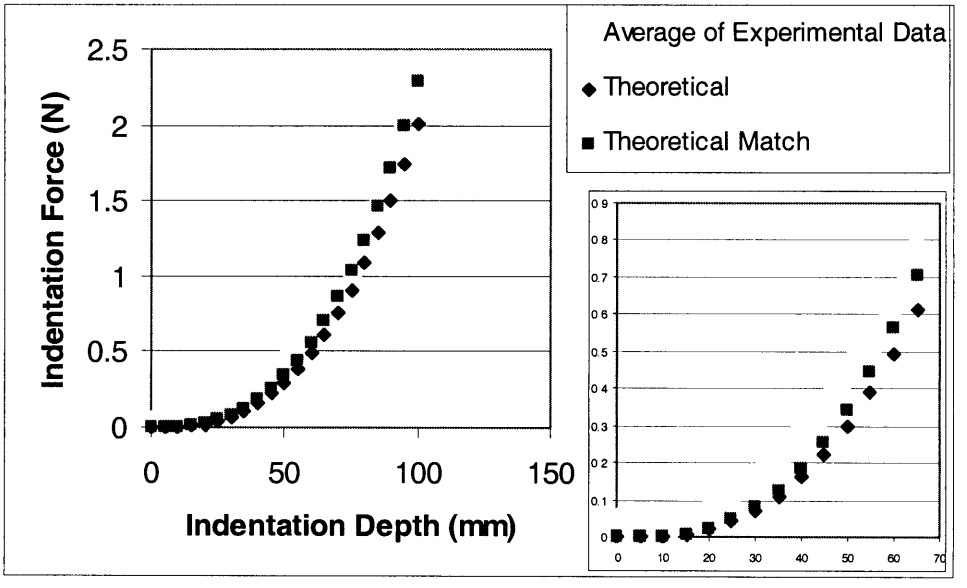

(a)

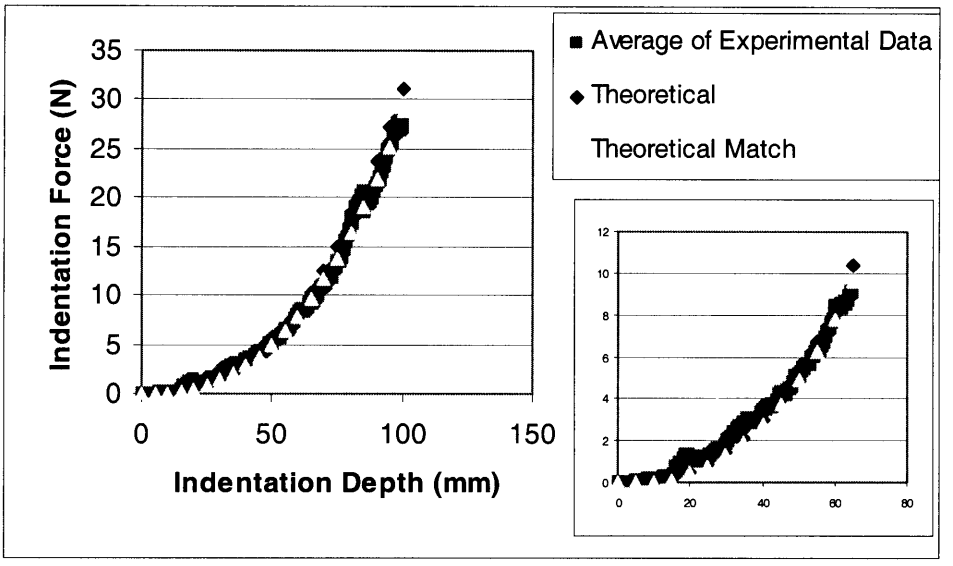

(b)

Figure 22: Comparison of theory and the average of the experimental data and contain blowup sections; (a) model B and 21.6° indenter; (a) model A and 21.6° indenter.

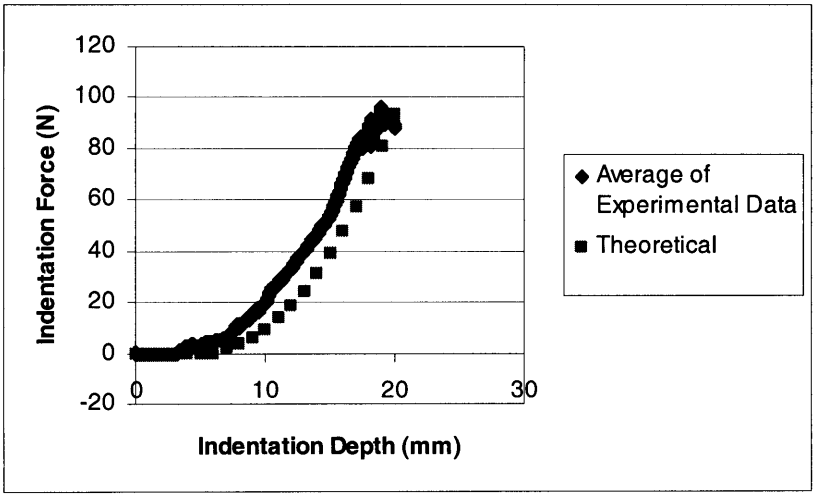

Figure 23: Comparison of theory and the average of the experimental data for model A and the 65.3° indenter.

For the particular combination, the edge effects had a greater impact on the results. The theory does not account for these edge effects and thus an accurate and meaningful match is not possible. When using 65.3° indenter with model B, the compression that occurred created artifacts too large to accurately match the theory and results. Further, taking the

average of the tests conducted was not a good representative measure of the experiments due to the consistent but random artifacts. But portions of the indentation results for a specific test reflected the predicted behavior at points when there were no tubes undergoing compression or other edge effects, as seen in figure 24.

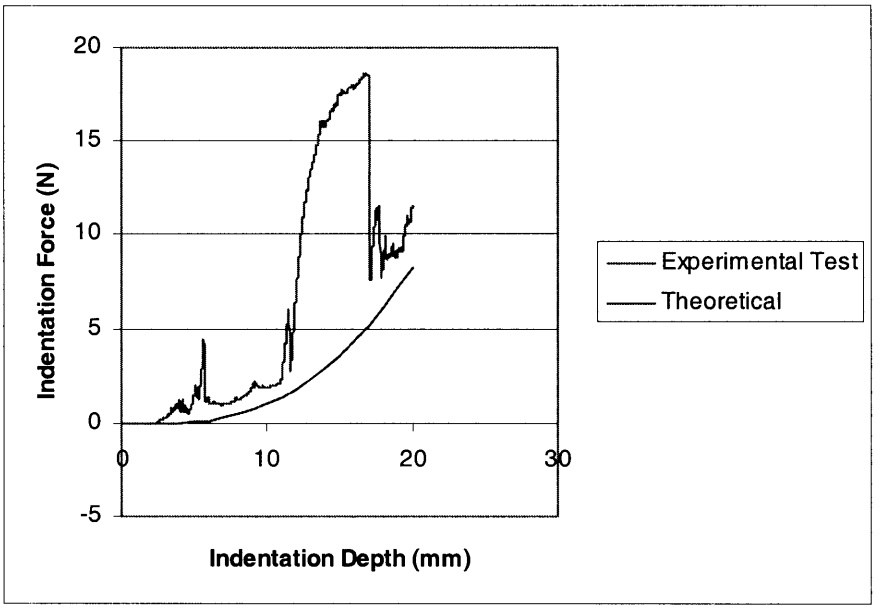

Figure 24: Comparison of theory and an experimental test for model A and the 65.3° indenter.

However, the combination of model B and the flatter indenter does not adequately support using indentation with the large angle indenter as a means to determine the elastic modulus of the tubes. In general, the denser the forest of tubes or the flatter the indenter the greater the potential there is for aberrations that will skew experimental data and lead to high errors when determining the elastic modulus for the material.

Also notable is the fact that the mechanical model of indentation assumes small angles of deflection for the tubes. When indenting to depths greater than ¾ the length of the tube, the behavior of the tubes does not necessarily follow small angle bending theory. Thus towards the later stages of indentation the experimental data deviates slightly from the theory.

5. Scratching

5.1 Introduction

The scratching of VACNTs has yet to be explored, but scratching is a likely cause for mechanical failure of nanoforests. For scratching, the indenter is positioned at a predetermined depth where it remains fixed. The forest of tubes, whether CNTs or a macro scale model as this paper addresses, are then moved horizontally while the indenter remains stationary. The initial position of the indenter acts as the zero point of the horizontal displacement, or scratch distance, x. As the forest of tubes is displaced, the tubes deflect with respect to the scratch distance and indenter angle.

The deflection of the tube, when the indenter is positioned at large depths relative to tube height, enters three phases with respect to the way it contacts the indenter. The first phase, end point contact and seen in figure 25, occurs when the angle of deflection is less than the angle of the indenter face. Here the indenter is in point contact with the tip of the tube. For such cases the deflection of the tube and subsequent force follow the same theory as indentation and is summed for each tube in contact with the indenter. As the sample is moved horizontally, the tube is further displaced proportional to the amount of horizontal displacement of the sample and the angle of contact the indenter makes with the tube with respect to the horizontal. Here the behavior of the tube follows the linear relationship of deflection versus force, as found in indentation, and the sum of all the tubes would be exponential. Once the angle of the deflection of a tube equals the angle of the face of the indenter the tube enters a period of line contact, phase two, with the indenter and can be seen in figure 26.

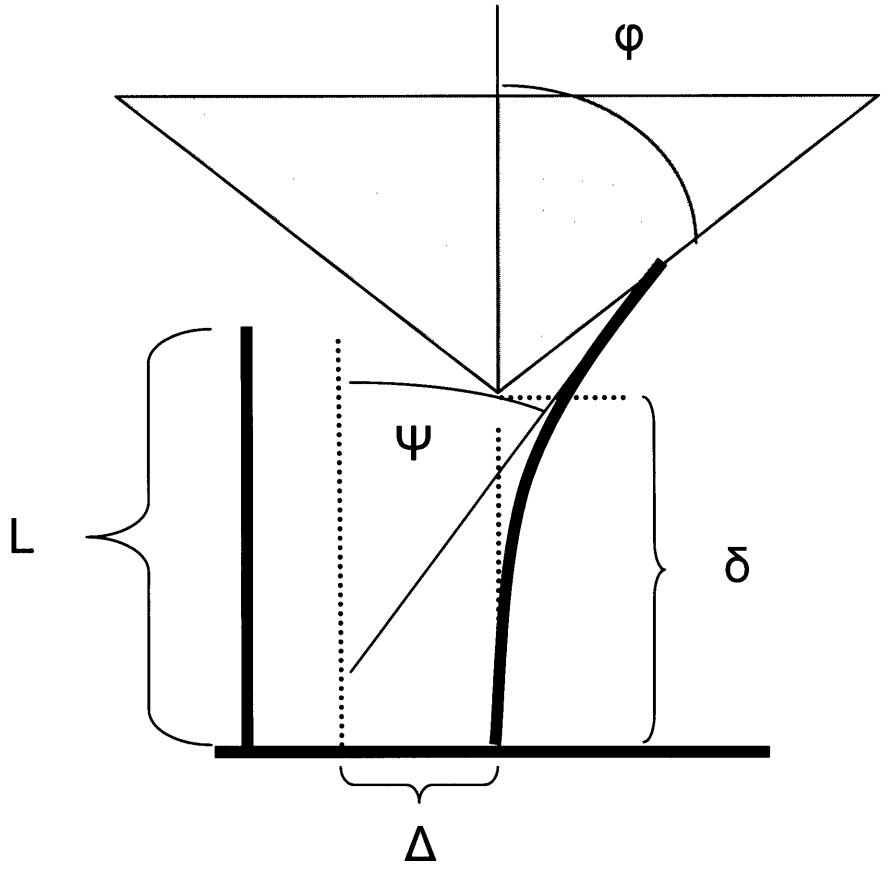

Figure 25: Phase one, end point contact, of scratching [11].

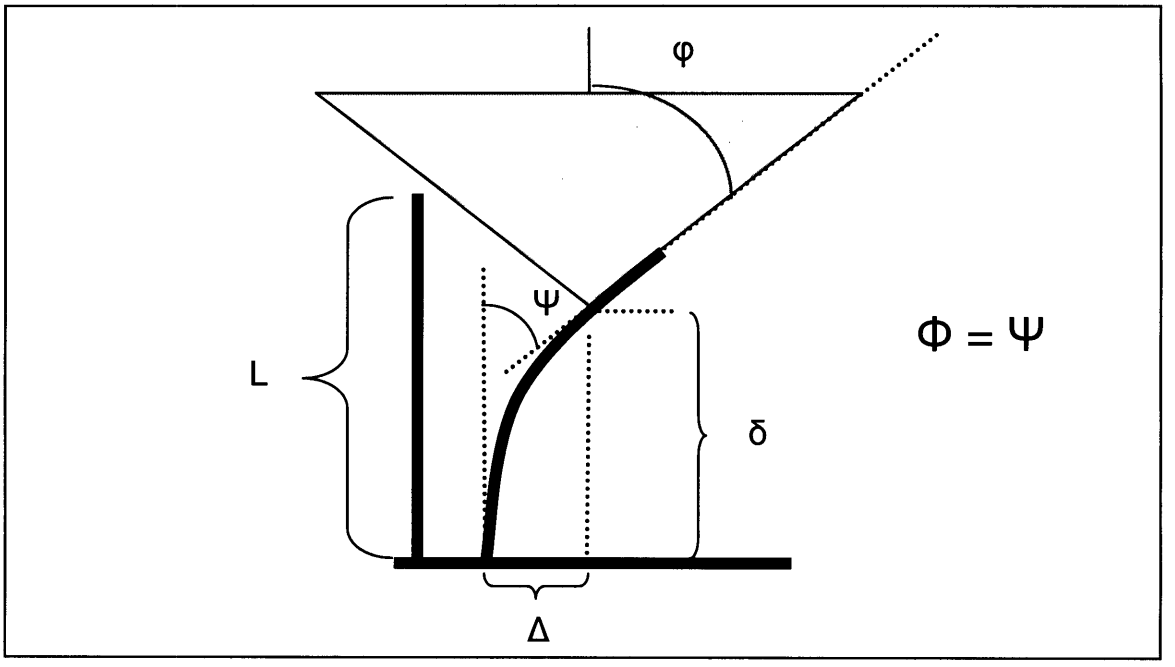

Figure 26: Phase two, line contact phase [11].

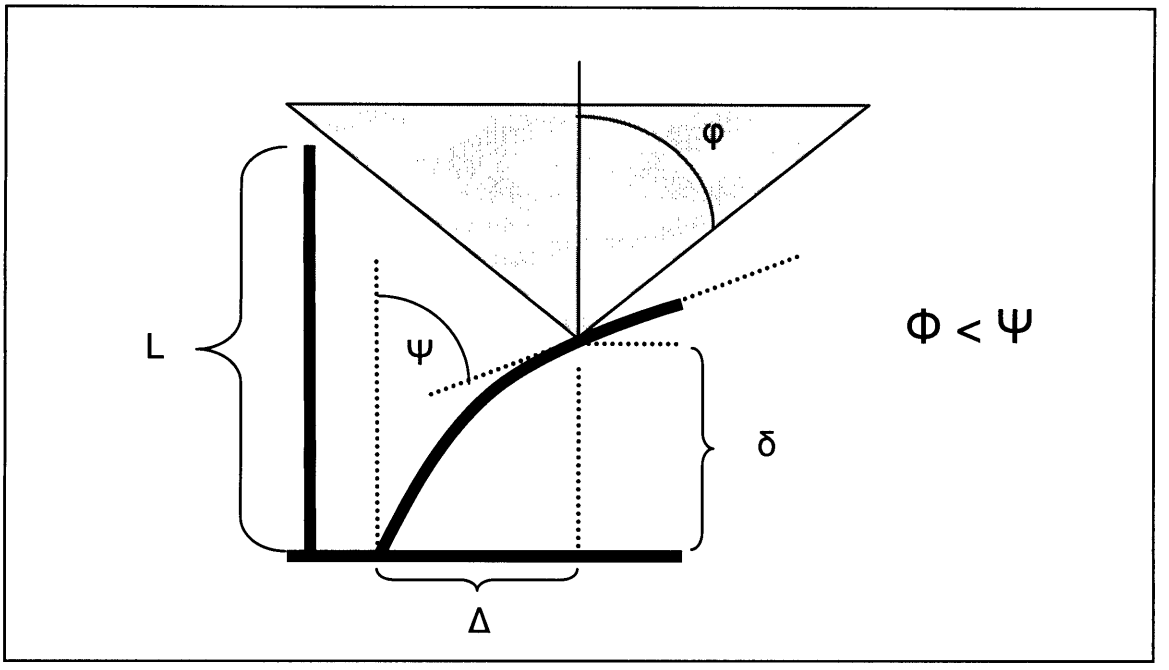

Figure 27: Phase three, point contact phase [11].

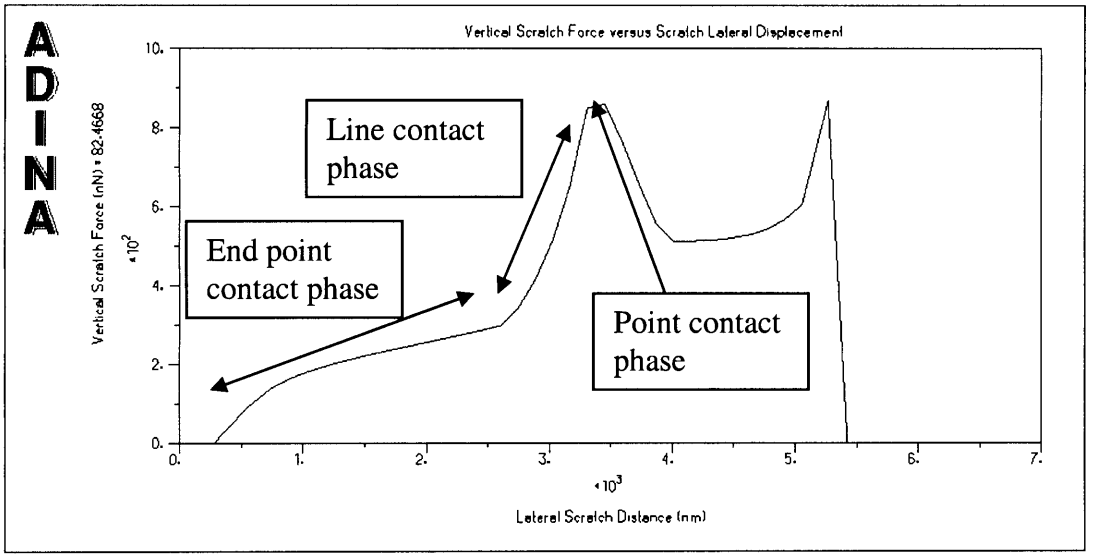

Figure 27: Theoretical prediction of scratching force verses scratching distance [11].

For tubes in this state, the relationship of force versus deflection is no longer linear, as determined by current numerical analysis being done. The tube exhibits an increase in the slope of the curve and even exhibits a bit of exponential behavior. The third phase, point contact, shown in figure 27, occurs when the deflection of the tube plus the angle of

the indenter equal 90°. Here the point of contact occurs at the lowest point of the line contact near the tip of the indenter and near the base of the tube [11]. Figure 28 shows a theoretical analysis of the potential behavior of scratching force verses the scratch displacement of a nanoforest model and when a tube undergoes each phase.

5.2 Results and discussion of macro-scaled scratching

Various scratching tests were conducted on the physical models in order to verify the shape of the scratching force versus scratching displacement. The tests were not used to verify numerical predictions at this point. Due to apparatus constraints, the model had to be pushed by hand and thus could only obtain curves for scratching force verses time. However, as scratching distance is proportional to time (distance = time * velocity, where velocity was kept rather constant) the shape of the curves can be compared to predicted behavior.

First a test was conducted on a single tube in order to isolate the behavior and determine whether in fact three phases of contact occur. Figure 29 shows a curve for scratch force versus time conducted on a tube from model A and clearly demonstrates all three phases. Figure 30 shows pictures of the tubes during each phase.

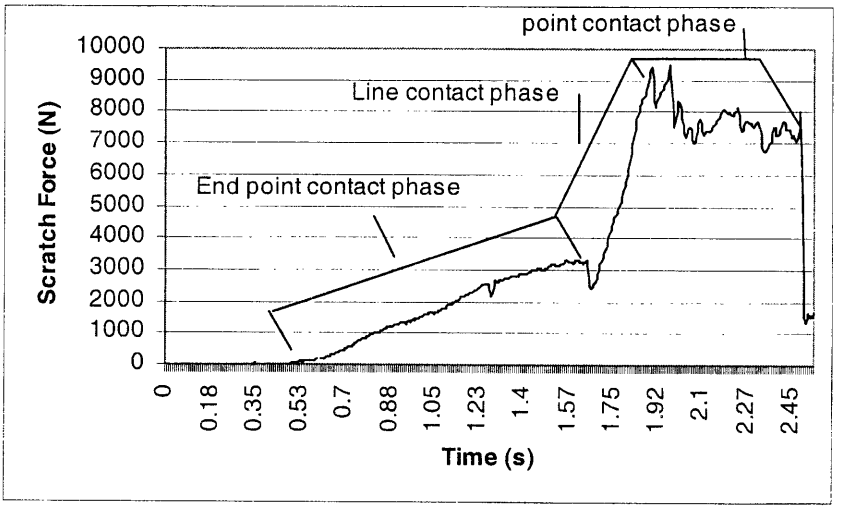

Figure 29: Scratch force versus time for a single tube of model A and the 21.6° indenter at a depth of 70 mm.

(a)

(b)

(c)

Figure 30: Photos demonstrating the three contact phases of scratching; (a) end point contact; (b) line contact; (c) point contact.

The curve certainly has a lot of noise, but that was due to friction on the surface of the indenter. When one tube of model B was tested (see Appendix C), the aberrations from friction were far more noticeable because of lower scratch resistance forces due to the smaller diameter and greater height. The third phase appears to be a bit different than theorized. Instead of the rounded parabolic top, indicating the point when the tube is

about to slip off the indenter completely, the curve shows more of a flat, constant force segment. However, when doing the experiment the speed was attempted to be kept constant but at these higher forces the speed began to slow down due to human error. Thus, there is little conclusive evidence that the behavior is in fact different. In general, the rough experiment proved that the theoretical model for scratching is accurate in behavior. One area that appears to differ a bit is the point right when the tube enters the line contact phase. Their appears to be a spike decrease in force before entering the line contact segment and is constant throughout the experiments and is also consistent when examining scratching for two tubes and for all the tubes.

The theoretical model proposed also examines the case for two tubes, as seen in figure 31 and was compared to experiments done using model B, seen in figure 32. The theoretical graph has two different models. The first model results were obtained using the finite element code, Abaqus, and the second model results were obtained using Matlab, where the equations describing the evolution of tube bending during scratching were programmed. Looking specifically at the Matlab model, the first tube follows the same initial behavior of one isolated tube, but as the second tube begins to touch the indenter, the scratch force shifts up.

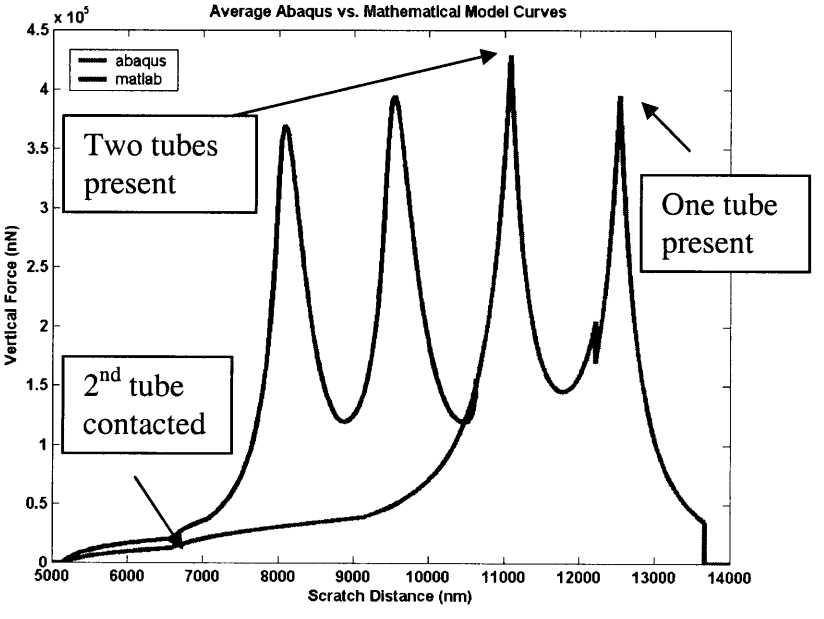

Figure 31: Theoretical graph of scratch force and time for two tubes.

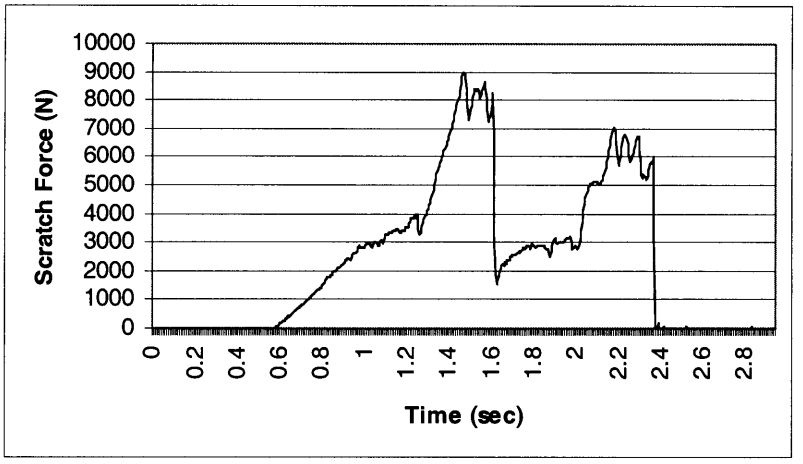

Figure 32: Scratch Force versus time for two tubes of model A and the 21.6° indenter at a depth of 70 mm.

The first peak, corresponding to the third phase, thus is taller than the second peak. In general, the experimental curves look very similar in nature and follow the predicted behavior for two tubes. Again the peak areas appear elongated but are most likely due to human error in moving the model and exhibit spikes due to friction.

Scratching was finally done for multiple tubes. Both macro scale models, A and B, were exposed to scratching. The scratch force versus time results do not clearly show the effect of isolated tube interactions because of the complexity introduced by all the tubes. However, some overall characteristics are still very evident.

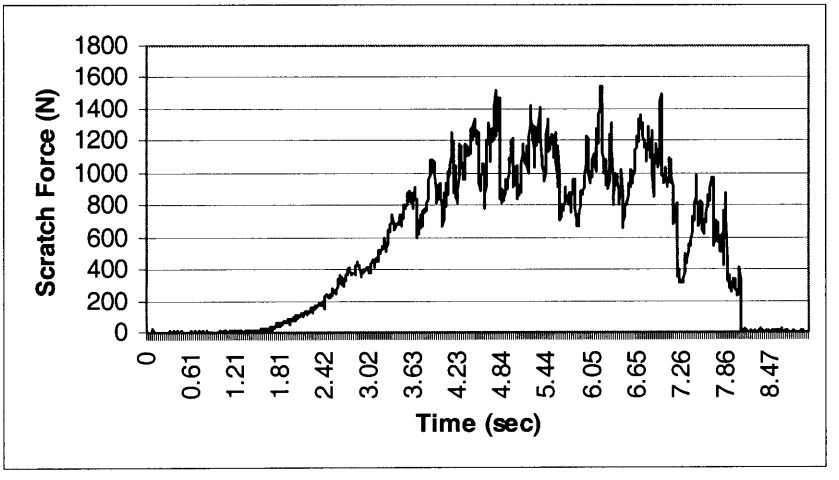

Figure 33: Scratch force versus time for all tubes of model B exposed to the 21.6° indenter at a depth of 80 mm.

The curve, seen in figure 33, is for model B (curve for model A is found in Appendix E and a photo of model A experiment in Appendix F), and instead of a linear progression of phase one for one tube, the force increases exponentially, which corresponds to indentation of multiple tubes. Once some of the tubes enter the second and third phases, the graph shows a series of spikes that in actuality show some isolated behavior consistent with that of a single tube or two tubes. The spikes occur due to the tubes slipping off the indenter and the new tubes engaging the indenter. However, some of the spikes may have been the result of frictional behavior and thus hard to distinguish between the two. In general, for better results, a linear stage, controlled by a constant speed motor, needs to be used and recorded for distance. Such an experiment would lead to more conclusive numerical results as well.

6. Conclusions

The macro scale physical model of nanoindentation certainly proved to be useful. For forests with low areal density combined combined with an indenter with a 21.6° face angle, the experimental data adequately predicts the elastic modulus of the material. While some error was evident, it was relatively small. The aberrations, mainly edge effects, responsible for the errors are probably found in nanoindentation, as similar shaped artifacts appear in the indentation force verses indentation depth curve of nanoforests. However, some of the aberrations were clearly more the result of problems with the model. The larger indenter created large edge effects. In nanoindentation the tops of the CNTs are actually spherical and thus most likely to become unstable quicker than the tubes did in the model; thus the aberrations would have a smaller and less noticeable effect. Further some of the inconsistencies on the face surface of the indenters created some isolated compression and thus more of a model specific error.

In general, as long as the aberrations are minimal, indentation appears to be an excellent method for determining the elastic modulus of materials. Experimental results that clearly show identifiable aberrations should be disregarded when determining the modulus. The frequency of the aberrations also suggest that indentation must not be

considered a consistent process for *some* combinations of forest density, height, length and indenter face angle and thus not reliable for determining moduli.

Researches believe that scratching may cause structural defects but no tests have yet to have been conducted on actual nanotubes. The experiments done on the macro scale physical models certainly begin to validate the theoretical predictions of the behavior some CNT researches expect. Specifically, the experiments exhibit behavior of three phases of contact between the indenter and tubes: end point contact, line contact and point contact. The single tube and two tube tests particularly demonstrated the behavior. The multiple tube experiments, however, need to be more thoroughly explored and observed and applied to a theoretical model that accounts for the parameters involved in the model.

Appendix A

```
function [stress2] = geoff_load

clear;
%Basic parameters Below%
E=(.7)*1.0e+9;    % N/m^2
Do=[3/16]*0.0254; % m
l=5.75*0.0254; %long tubes%
% l=(12.78)*Do;     % m% , %short tubes%
I=pi*(Do^4)/64;
stiffness=E*I;
% phi=21.6*pi/180; %for sharp indenter%
phi=65.3*pi/180;  %flat indenter%
theta = 30.0*pi/180;
hmax=.02 %flat indenter%
% hmax=.1; %sharp indenter%
% m =.7/(0.0254)^2; % # / m^2% $short tubes%
m=1.46/(0.0254)^2; % # / m^2% $long tubes%

h1 = 0;
nh = 20;
dh = hmax/nh;

for z=1:(nh+1)
   h(z)=h1+dh*(z-1);
%     A(z)=0.813*(h(z))^2+4.11*Do*h(z)+3.141.*Do.^2; %sharp indenter%
   A(z)=24.56*h(z)^2
   num_cnt(z)=A(z)*m;
   num_cnt(z) = floor(num_cnt(z));
end

pmax = 0;
defmax = 0;

for i = 1:(nh+1)
   pp = 0;
   hf = h(i);
   num_c = num_cnt(i);
   for j = 1:num_c
        A=j/m;
%          hi(j)=(sqrt(((4.11.*Do).^2-(4.*(3.141*Do.^2-A).*.813)))-4.11.*Do)./(2.*.813);
%sharp indenter%
        hi(j) = sqrt(A/24.56) %flat indenter%
      x=(hf-hi(j));
```

```
      if x<0
         x=0;
      end
      deflection = x*tan(phi);
      p = point_load(deflection,l,stiffness,phi);
      pp = pp + p;
      if (hf == hmax)
         if (p > pmax)
            pmax = p
            if (deflection > defmax)
               defmax = deflection;
               if (j == num_cnt)
                  p = pmax;
                  deflection = defmax;
               end
            end
         end
      end
   end
%    hhh(i) = hf/.0254; % inches%
   hhh(i) = hf*1000
   force(i) = pp
%    force(i) = pp/9.81*2.2 %lbs%
end

%Finding Stress for each tube at base where y=0%
T=p/tan(phi);
stress=((T.*l+p.*deflection).*(Do./2)./I)-(p./(pi.*((Do./2).^2)));
stress2=((T.*l+p.*deflection).*(Do./2)/I);
stress3=(T.*l.*(Do./2))/I ;

figure(1);
plot(hhh(:),force(:),'r');
xlabel('depth (mm)');
ylabel('force (N)');



function p = point_load(deflection,length,stiffness,phi)
A = 1/tan(phi);
guess = sqrt(1/stiffness); % guess for effective stiffness %
tol = 1e-10; % tolerence%
k = newton_ralphson(deflection,A,length,guess,tol);
p = stiffness.*k.^2;
```

```
function k = newton_ralphson(def,A,len,guess,tol)
kn = guess;
del_kn = ((A.*tan(kn.*len)-A.*kn.*len-
(kn.*def)).*(kn.*(cos(kn.*len)).^2))./(A.*(sin(kn.*len).*cos(kn.*len)-kn.*len));
kn1 = kn + del_kn;
while (abs(kn1-kn) > tol)
   kn = kn1;
   del_kn = ((A.*tan(kn.*len)-A.*kn.*len-
(kn.*def)).*(kn.*(cos(kn.*len)).^2))./(A.*(sin(kn.*len).*cos(kn.*len)-kn.*len)); % = -
del(kn)./(dM/dk)
   kn1 = kn + del_kn;
end
k = kn1;
```

Appendix B

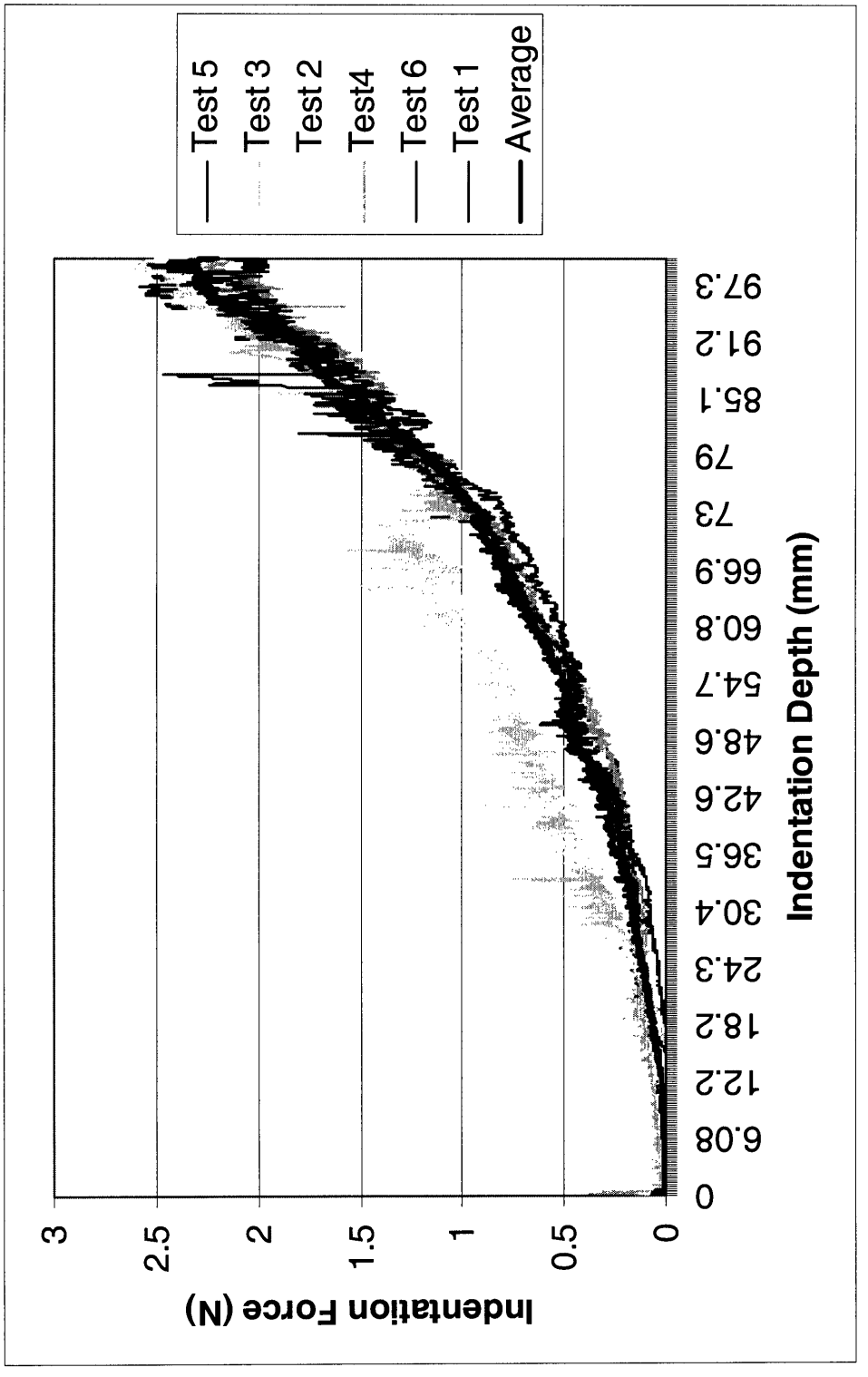

Figure 34: Indentation force versus depth for model B with 21.6° indenter and includes all tests taken and average of tests.

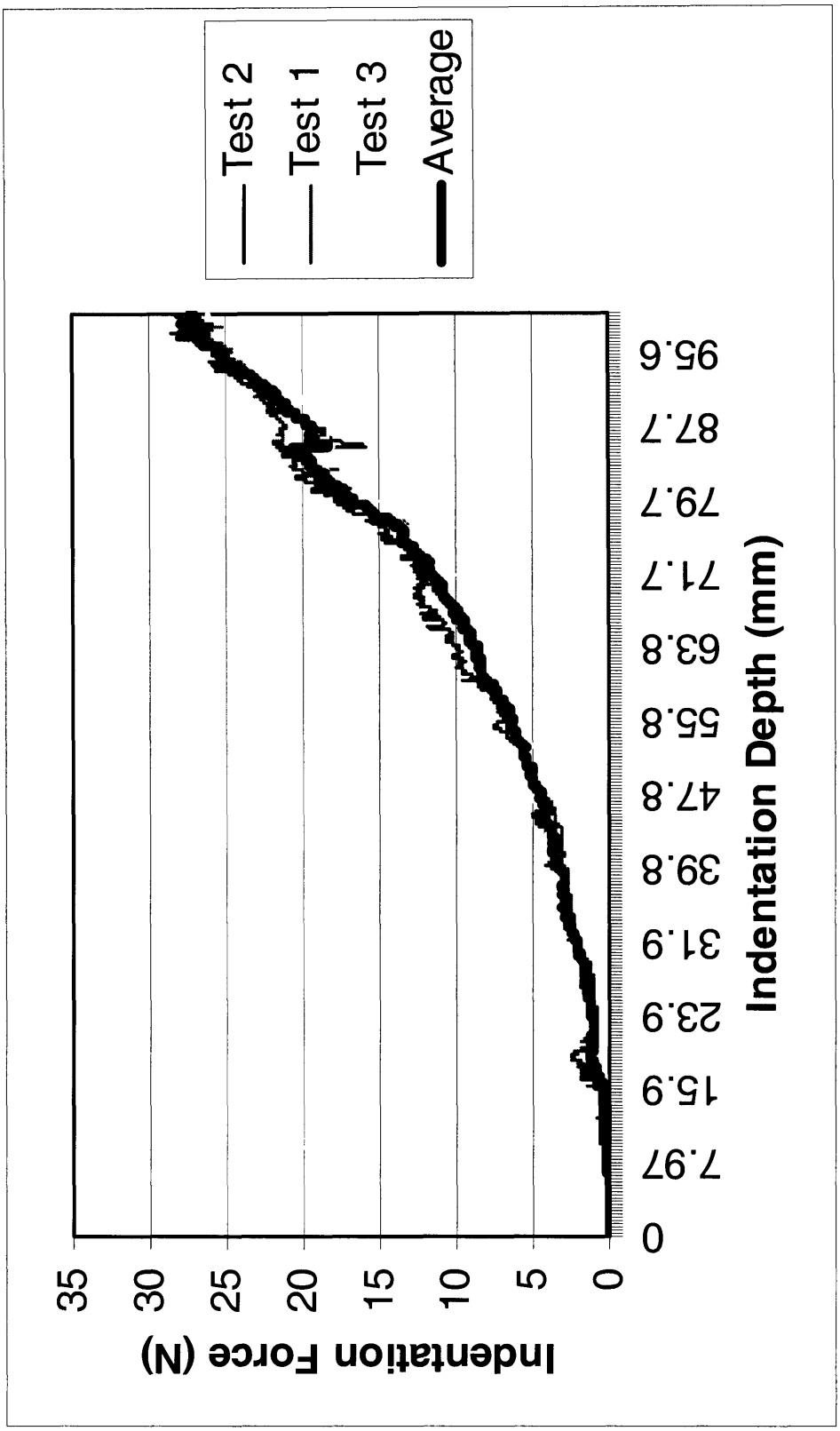

Figure 35: Indentation force versus depth for model A with 21.6° indenter and includes all tests taken and average of tests.

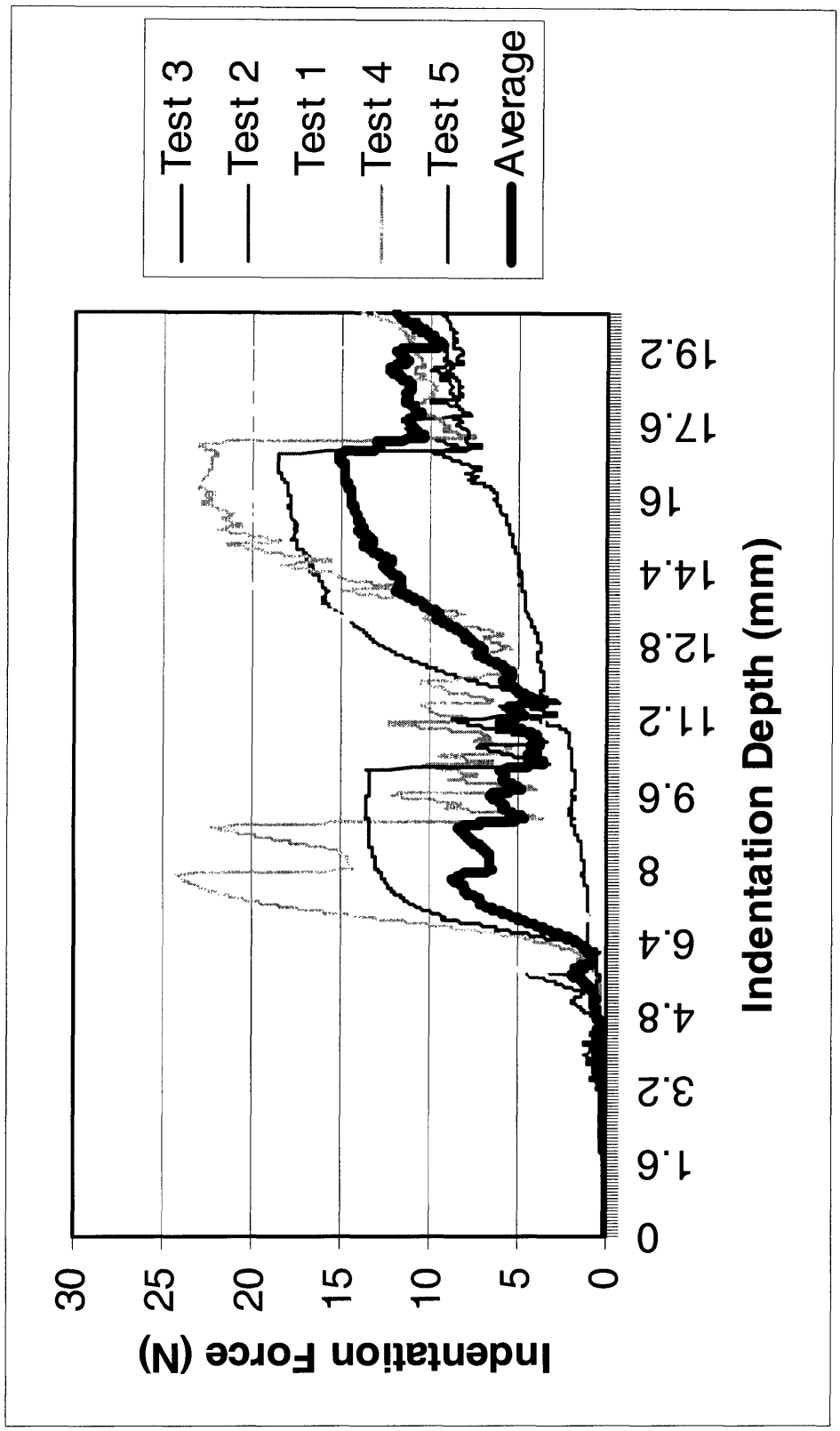

Figure 36: Indentation force versus depth for model B with 65.3° indenter and includes all tests taken and average of tests.

Appendix C

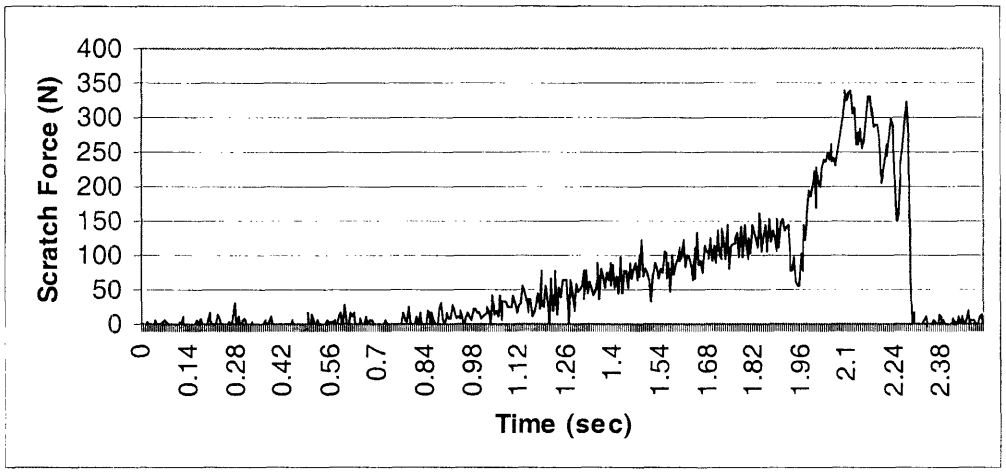

Figure 37: Scratch test for model B and 21.6° indenter at a depth of 80 mm.

Appendix D

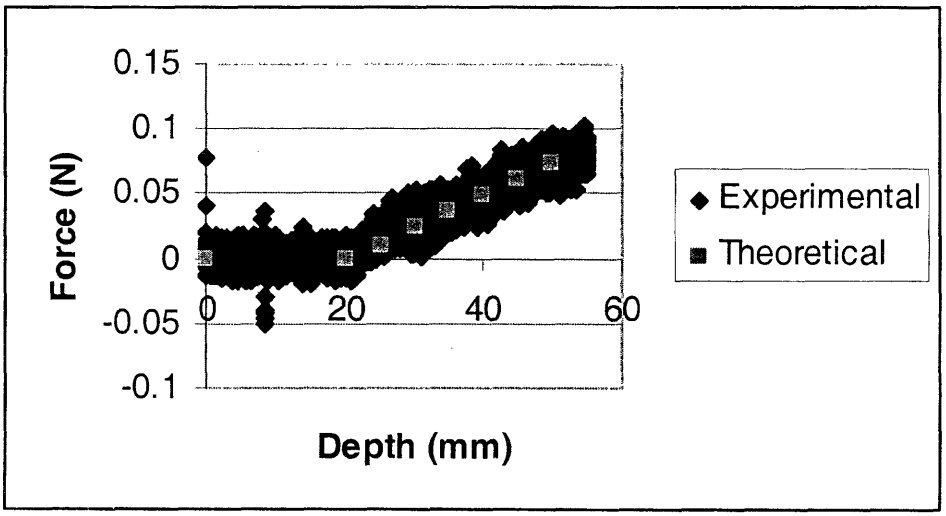

Figure 38: Indentation for a single tube and compared to theoretical. Test used to confirm an elastic modulus of 0.7 GPa

Appendix E

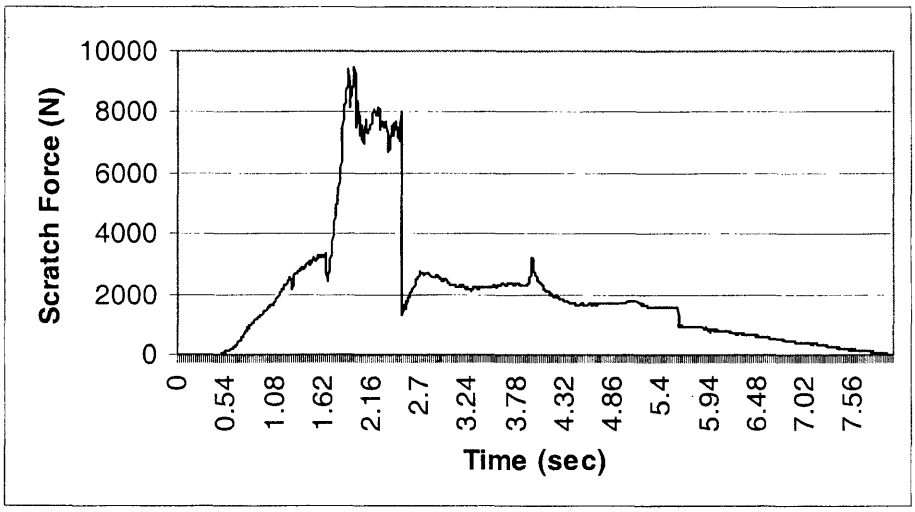

Figure 39 Scratch force versus time for all tubes of model B exposed to the 21.6° indenter at a depth of 70 mm.

Appendix F

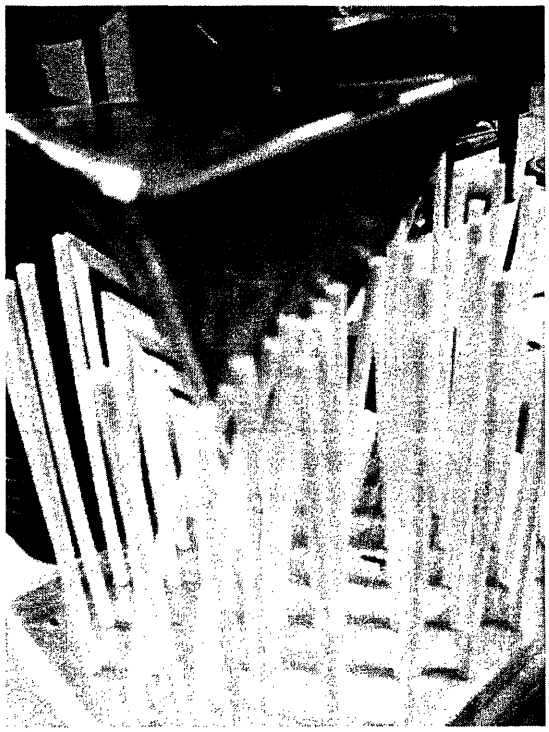

Figure 39: Photo of scratching for all tubes of model B using the 21.6° indenter.

References

[1] Qi, H.J., Teo, K.B.K., Lau, K.K.S., Boyce, M.C., Milne, W.I., Robertson, J., Gleason, K.K., 2003. Determination of mechanical properties of carbon nanotubes and vertically aligned carbon nanotube forests using nanoindentation. Journal of the Mechanics and Physics of Solids. 51, 2213-2237.

[2] Treacy, M.M.J., Ebbesen, T.W., Gibson, J.M., 1996. Exceptionally high Young's modulus observed for individual carbon nanotubes. Nature 381, 678.

[3] Wong, E.W., Sheehan, P.E., Lieber, C.M., 1997. Nanobeam mechanics: elasticity, strength, and toughness of nanorods and nanotubes. Science 277, 1971 1975.

[4] Poncharal, P., Wang, Z.L., Ugarte, D., de Heer, W.A., 1999. Electrostatic deflections and electromechanical resonances of carbon nanotubes. Science 283, 1513-1516.

[5] Salvetat, J.P., Bonard, J.M., Thomas, N.H., Kulik, A.J., Forro, L., Benoit, W., Zuppiroli, L., 1999. Mechanical properties of carbon nanotubes. Applied Physics A 69, 225-260.

[6] Pantano, A., Parks, D.M., Boyce, M.C., 2003. Mechanics of deformation of single- and multi-wall carbon nanotubes. Journal of the Mechanics and Physics of Solids. 52, 789-821.

[7] Pantano, A., Boyce, M.C., Parks, D.M., 2004. Mechanics of axial compression of single- and multi-wall carbon nanotubes. Journal of Engineering Materials and Technology, in press.

[8] Yakobson, B., Brabec, C., Bernholc, J., 1996. Nanomechanics of carbon tubes: instabilities beyond the linear response. Physics Review Lett. 76 (14), 2511-2514.

[9] Zhou, X., Zhou, J.J., Ou-Yang, Z.C., 2000. Strain energy and Young's modulus of single-wall carbon nanotubes calculated from electronic energy-band theory. Physics Review B 62 (20), 13692-13696.

[10] Tu, Z., Ou-Yang, Z., 2002. Single-walled and multi-walled carbon nanotubes viewed as elastic tubes with the effective Young's modulus dependent on layer number. Physics Review B 65, 233407.

[11] Garg, M; research done in partial fulfillment of S.M. of Mechanical Engineering at Massachusetts Institute of Technology. Personal contact, 2004.